AFRL-AFOSR-JP-TR-2019-0022

Template Effect on Guiding Biomolecular Growth by 3-D Carbon Nanotube Networks on Silicon and Quartz Plates

Haiwon Lee
HANYANG INDUSTRY-UNIVERSITY COOPERATION
HAENGDANG 1DONG, SEONGDONG-GU, SEOULRM110. HIT, HANYANG UNIV.
17
SEOUL, 133-791
KR

03/26/2019
Final Report

REPORT DOCUMENTATION PAGE		Form Approved OMB No. 0704-0188

The public reporting burden for this collection of information is estimated to average 1 hour per response, including the time for reviewing instructions, searching existing data sources, gathering and maintaining the data needed, and completing and reviewing the collection of information. Send comments regarding this burden estimate or any other aspect of this collection of information, including suggestions for reducing the burden, to Department of Defense, Executive Services, Directorate (0704-0188). Respondents should be aware that notwithstanding any other provision of law, no person shall be subject to any penalty for failing to comply with a collection of information if it does not display a currently valid OMB control number.
PLEASE DO NOT RETURN YOUR FORM TO THE ABOVE ORGANIZATION.

1. REPORT DATE (DD-MM-YYYY) 26-03-2019	2. REPORT TYPE Final	3. DATES COVERED (From - To) 22 Sep 2015 to 21 Nov 2018

4. TITLE AND SUBTITLE	5a. CONTRACT NUMBER
Template Effect on Guiding Biomolecular Growth by 3-D Carbon Nanotube Networks on Silicon and Quartz Plates	
	5b. GRANT NUMBER FA2386-15-1-4081
	5c. PROGRAM ELEMENT NUMBER 61102F
6. AUTHOR(S) Haiwon Lee	5d. PROJECT NUMBER
	5e. TASK NUMBER
	5f. WORK UNIT NUMBER

7. PERFORMING ORGANIZATION NAME(S) AND ADDRESS(ES) HANYANG INDUSTRY-UNIVERSITY COOPERATION HAENGDANG 1DONG, SEONGDONG-GU, SEOULRM110. HIT, HANYANG UNIV. 17 SEOUL, 133-791 KR	8. PERFORMING ORGANIZATION REPORT NUMBER

9. SPONSORING/MONITORING AGENCY NAME(S) AND ADDRESS(ES) AOARD UNIT 45002 APO AP 96338-5002	10. SPONSOR/MONITOR'S ACRONYM(S) AFRL/AFOSR IOA
	11. SPONSOR/MONITOR'S REPORT NUMBER(S) AFRL-AFOSR-JP-TR-2019-0022

12. DISTRIBUTION/AVAILABILITY STATEMENT
A DISTRIBUTION UNLIMITED: PB Public Release

13. SUPPLEMENTARY NOTES

14. ABSTRACT
The PI was successful at their grant research. In the first year the researchers fabricated idfferent types of 3D carbon nanotube curtains on silican pillar substrates. They were also able to functionalize the surface to template the growth of biomaterials. The second year was spent to develp the nanotube web structure as a biosensor platform. The researchers successfully modified the nanotube walls with RF plasma treatment adn were able to create a strech sensor. In the third year, the PI was able to create a simple an defficient label free bacterial dections system. 4 peer reviewed papers were a direct result of this grant award.

15. SUBJECT TERMS
Nanopillar arrays, Carbon Nanotube (CNT) Scaffolds, Neurons, Microfluidics, Surface Chemistry

16. SECURITY CLASSIFICATION OF:			17. LIMITATION OF ABSTRACT	18. NUMBER OF PAGES	19a. NAME OF RESPONSIBLE PERSON CHEN, JERMONT
a. REPORT	b. ABSTRACT	c. THIS PAGE			
Unclassified	Unclassified	Unclassified	SAR		19b. TELEPHONE NUMBER (Include area code) 315-227-7007

Standard Form 298 (Rev. 8/98)
Prescribed by ANSI Std. Z39.18

Template Effect on Guiding Biomolecular Growth by 3-D Carbon Nanotube Networks on Silicon and Quarts Plates

Name of Principal Investigator: Haiwon Lee

- e-mail address: haiwon@hanyang.ac.kr

- Institution: Hanyang University

- Mailing. address: Department of Chemistry, Hanyang University,
  222 Wangshimni-ro, Seongdong-gu, Seoul 04763, Korea

- Phone: +82-2-2220-0945

- Fax: +82-2-2296-0287

Period of Performance: 09/22/2015 – 09/21/2018

1. First Year Progress Report

We focused on fabrication of different kind of 3D CNT curtain (3DCNC) structures on silicon pillar assisted substrates and CNT surface modification or functionalization for biomolecule growth applications. The designing of different Si pillars is shown in Scheme 1. By using atomic layer deposition (ALD), a 3D CNT web (3DCNW) structure was well coated with a layer of Al_2O_3. Followed with 3-(2-aminoethylamiano) propyldimethoxymethylsilane (AEAPDMS) self-assembly process, the CNT/Al_2O_3 surface were successfully modified with amine groups (-NH_2). The surface modification of CNT for generating amine groups by plasma treatment seems to be an easy and less-disruptive process. By combining acetylene plasma pretreatment and ammonia plasma treatment the CNT surface are more effectively functionalized with amine groups. In addition, polyaniline (PANI) coated 3DCNW embedded in hydrogels was fabricated as a template for guiding the growth of biomaterials.

1.1. Aligned PANI/3DCNW hybrid for cell growth

Introduction

Traditional neural interfaces using metallic electrodes have many problems such as high impedance, mechanical mismatch. These problems result in unstable electrical stimulation of tissue such as cell damage and foreign body response. To resolve these problems, blending hydrogels with conductive components like CNTs or conductive polymers have enormous potential in medical electrode application due to low impedance. Conductive hydrogel materials have been proven that there are negligible cytotoxicity and good biocompatibility in vitro with a few cell types. The biological characteristic of conductive hydrogels shows the characteristic of the component polymers, which have been reported to be compatible with a range of cell types. Specifically, conductive hydrogel biomaterials have been used to aid the attachment and growth of PC12 cells, the Schwann cells and the interleukin-3 dependent pro-B cell line (BaF_3). Development of the electrode interfacing material with an elastic modulus close to nerve tissue is necessary. There have been several recent reports to reduce the stiffness of electrodes. Several conductive hydrogel systems have been demonstrated to decrease the stiffness of electrodes, as anticipated the young's modulus of these hybrids generally lies between that of the component conductive polymer and hydrogel. Therefore, in this work, chemically synthesized conductive polymers were used as a component of a conductive hydrogel to control the amount of conductive polymer and have effect on both the electrical conductivity and stiffness of the hybrid. We developed a simple method by transferring aligned 3DCNW to hydrogel. And we showed that stiffness of the conductive hydrogel was similar to the native tissue from a whole embryonic forebrain.

Experimental

Synthesis of aligned CNTs

Aligned 3DCNW was synthesized on Si pillar substrate and randomly distributed CNTs was synthesized on flat Si substrate. The Si pillar structure with diameter of 2 μm, height of 5 μm was prepared. And the pillar gap of x-axis and y-axis is respectively 2 and 700 μm, as shown in Scheme 1e. Detailed CNT synthesis process has been explained in our previous works.

Coating polyaniline on aligned 3DCNW
PANI was coated by chemical method in solution. To control thickness of PANI, three substrates of aligned 3DCNW was prepared. Detailed synthesis process has been explained in our previous works. Three templates were respectively taken out from the solution after 15, 30, and 50 minutes dipping.

Fabrication of soft and conductive hydrogel
To fabricate the soft and conductive hydrogel, firstly gel solution was poured on synthesized PANI/3DCNW between micro pillar structures. The gel solution is prepared by mixing acrylamide, N, N′-methylenebisacrylamide, ammonium persulfate, and N,N,N′,N′-tetramethylethylenediamine (TEMED) in phosphate-buffered saline (PBS) solution. The composition of the gel is given by 20%T, 2.6%C (T = Total concentration of acrylamide and bisacrylamide monomer, C = bisacrylamide concentration). As %T is higher, the pores size of the gel is smaller. Polymerization was initiated by adding 20 μl of APS (10%) and 4 μl of TEMED as a catalyst. After gelation, this gel was detached on micro-pillar structure.

2D cell culture
To facilitate cell adhesion, 100 μg/mL Poly-D-lysine hydrobromide (PDL) (Sigma) was coated on the soft and conductive hydrogel in the incubator (37°C, 5% CO_2) for 3 hr. After removing the coating solution, the soft and conductive hydrogel was washed with PBS three times. To preparing cell seeding, Enzyme mixture 1 and 2 were firstly prepared. Buffer X 1750 μL and enzyme T 200 μL was used to make Enzyme mixture 1. Also, buffer Y 20 μL and enzyme A 10 μL was used to make Enzyme mixture 2. Secondly, after euthanizing pregnancy SD rat, embryo's brain was obtained. Also, after removing the midbrain and meninges, cortices were collected in the cold HBSS (Lonza) in conical tube. The collected cortices were centrifuged at 300 g for 3 min. And the supernatant was removed. Preheated enzyme mixture 1 was added and incubated at 37°C water bath for 15 min under continuous rotation. Also, enzyme mixture 2 was added and again incubated at 37°C water bath for 10 min under continuous rotation. They were dissociated using the other three fire-polished pasteur pipets and incubated at 37°C water bath for 10 min under continuous rotation. After adding preheated culture media, dissociated cells were filtered using 40 μm cell strainer. These cells were centrifuged at 300 g for 10 minutes and the supernatant was removed. The dissociated cells were counted using a hemocytometer. The Final cell density 4×10^6 cells/mL was prepared. These cells were seeded on the PDL coated hydrogel.

3D cell culture

Firstly, 2 mg/mL poly-dopamine was coated the soft and conductive hydrogel for 3 hrs. After removing the coating solution, the soft and conductive hydrogel was washed with PBS three times. Secondly, the collagen 0.25% (w/v) was diluted with 10x DMEM and DMEM. The pH of the collagen solution was adjusted to pH 7.4 by the addition of 0.5 N NaOH. Like 2D cell culture, cells were prepared and counted. And the Final cell density 4×10^6 cells/mL was prepared. These cells were mixed with collagen. Mixed collagen was poured on poly-dopamine coated hydrogel. After gelation in the incubator (37°C, 5% CO_2) for 30 min, culture media was added and exchanged with fresh culture media at every 2 days.

Results and Discussion
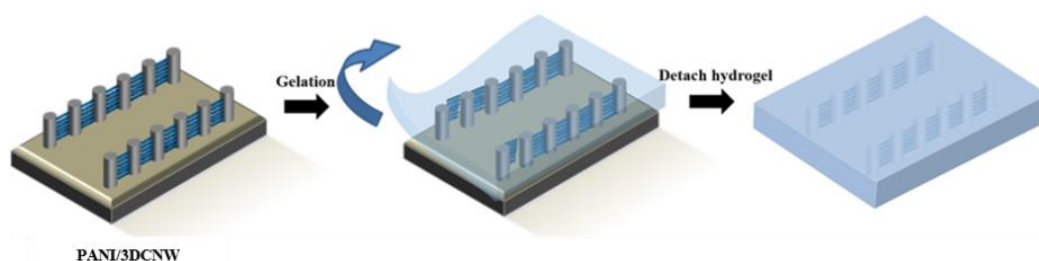
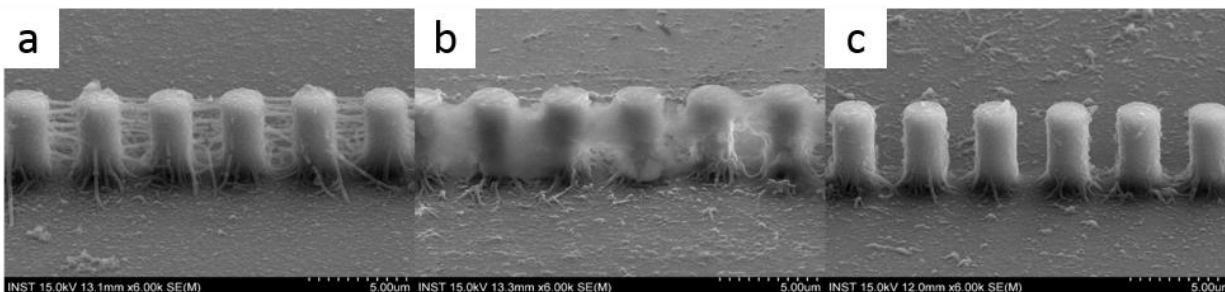Scheme 1. Schematic illustrations of the fabrication of conductive hydrogel for biomaterials.

Figure 1. The SEM images of (a) aligned PANI/3DCNW on Si pillar substrates after detaching hydrogel depending on the concentration of PAAm hydrogel (b) 10 wt% , and (c) 20 wt%.

Aligned PANI/3DCNW were simply transferred within PAAm hydrogel by detaching the hydrogel as shown scheme 1. As presented in Figure 1, the PAAm hydrogel concentrations of 10 and 20 wt% were prepared to select mechanically appropriate hydrogel and respectively detached to transfer aligned PANI/3DCNW within PAAm hydrogel. Figure 1b showed that a lot of residue remains on the Si pillar substrates. But residue of the PAAm hydrogel 20 wt% concentrations do not remain on the Si pillar substrates, as shown in Figure 1c. As a result, the PAAm hydrogel concentrations of 20 wt% is sufficient to transfer aligned PANI/3DCNW within PAAm hydrogel. In order to compare the conductivity, pristine 3DCNW, PANI-3DCNW with different thickness of PANI, and randomly distributed PANI-CNTs were prepared, respectively. The conductivity of 3DCNW/PAAm hydrogel and PANI-3DCNW/PAAm hydrogel were compared in Figure 2e. As a result, the conductivity of PANI/3DCNW/PAAm hydrogel was

higher than CNTs/PAAm hydrogel. And in order to control the thickness of aligned PANI/3DCNW bundles and compare the conductivity, three of the samples were respectively dipped in polymerizing aniline solution for 15, 30 and 50 min, as shown in Figure 2a, 2b, 2c, and 2d. The longer the reaction time, the thickness of aligned PANI-CNTs bundles became thicker. The conductivity of thick PANI-CNTs bundle within the PAAm hydrogel was higher than thin PANI/3DCNW bundle within the PAAm hydrogel (Figure 2e). In other words, as the thickness of aligned PANI/3DCNW bundles increased, the conductivity increased. Finally, the conductivity of aligned PANI/3DCNW/PAAm hydrogel and randomly distributed PANI-CNTs/PAAm hydrogel were compared (Figure 3a and 3b). As a result, the electrical conductivity of the aligned PANI/3DCNW/PAAm hydrogel was 100 times higher than randomly distributed PANI-CNTs/PAAm hydrogel. Because the current could be passed (Figure 3c).
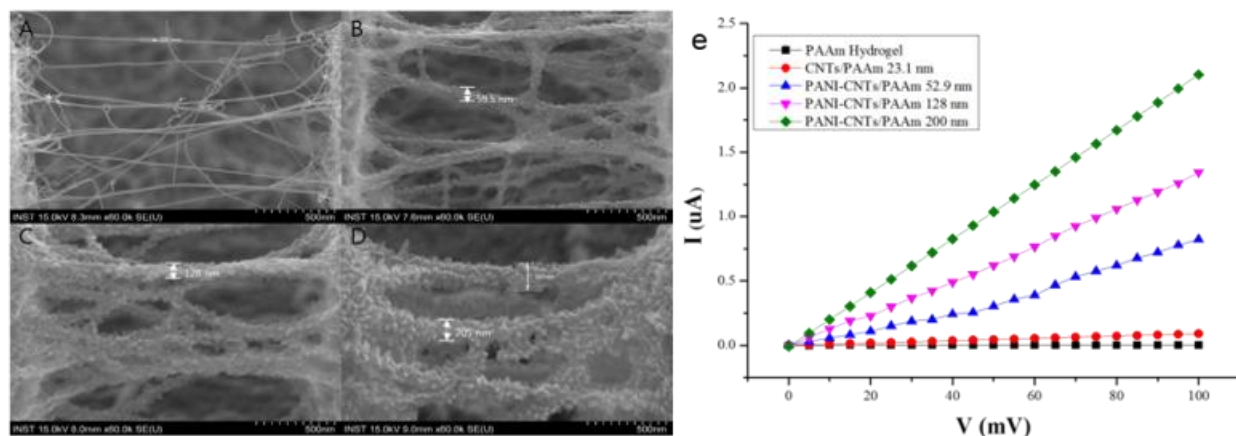

Figure 2. The SEM images of CNTs or PANI-CNTs bundle suspended between two pillars in different dipping time in solution. (A) Before dipping, (B) 15 min, (C) 30 min, (D) 50 min after dipping in polymerizing aniline solution. (E) Current-Voltage (I-V) curves of PANI-CNTs/PAAm hydrogel with different thickness of PANI-CNTs bundle, along with PAAm hydrogel and CNTs/PAAm hydrogel.
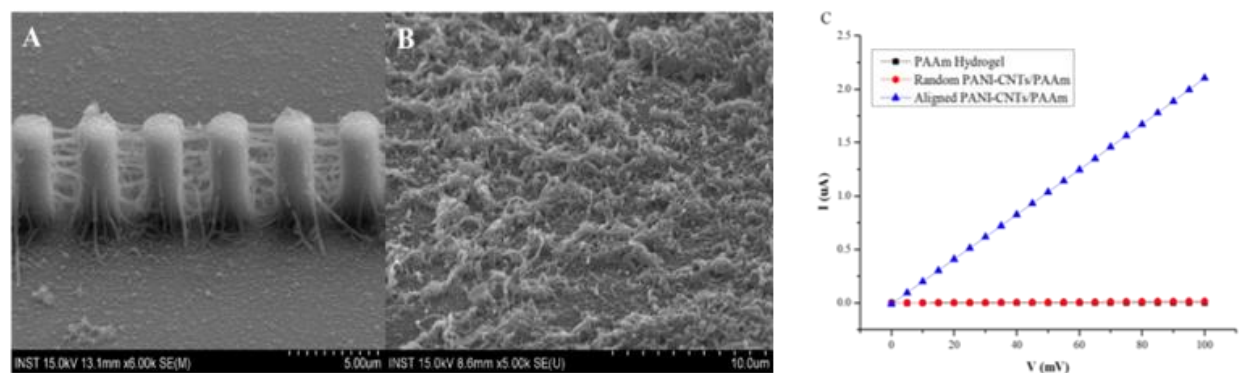

Figure 3. The SEM images of (A) aligned PANI/3DCNW on Si substrate and (B) randomly distributed PANI-CNTs on flat Si substrate. (C) Current-Voltage (I-V) curves of randomly distributed or aligned PANI/3DCNW /PAAm hydrogel along with PAAm.

A micromechanical mapping technique was used by the AFM to measure the mechanical properties of the hybrid aligned PANI/3DCNW/PAAm hydrogel. The hydrogel was reinforced with aligned PANI/3DCNW, its young's modulus increased from 1.18 ± 0.06 kPa to 3.61 ± 0.81 kPa as shown Figure 4. As a result, the stiffness of aligned PANI/3DCNW/PAAm hydrogel was 3

times higher than pristine hydrogel. The increase of Young's modulus was likely due to the formation of a well-connected 3D web structure within PAAm hydrogel. PANI/3DCNW alignment most likely caused a reinforcement between the PANI/3DCNW bundles. The mechanical properties of biomaterials affect cell adhesion, proliferation, and differentiation. Therefore, hydrogels with tunable mechanical properties are beneficial for use as biomaterials. Although the stiffness of PAAm hydrogels containing aligned PANI/3DCNW was increased, it is still similar to the native tissue from a whole embryonic forebrain. Therefore, they could be ideal biomaterials for soft tissues.
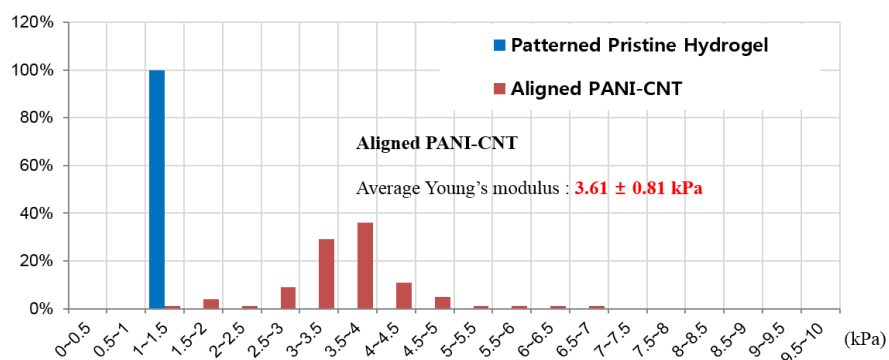

Figure 4. Mechanical properties of aligned PANI/3DCNW/PAAm hydrogel and patterned pristine hydrogel, as measured by AFM (in liquid). Young's modulus histogram.

Live/Dead assay was also performed on neural seeded directly and indirectly on hybrid aligned PANI/3DCNW/PAAm hydrogel, as shown in Figure 5 and Figure 6. The cell viability of both randomly distributed PANI-CNTs/PAAm hydrogel and aligned PANI/3DCNW/PAAm hydrogel were respectively compared in 2D and 3D cell culture. All cell viability was approximately more than 80%.
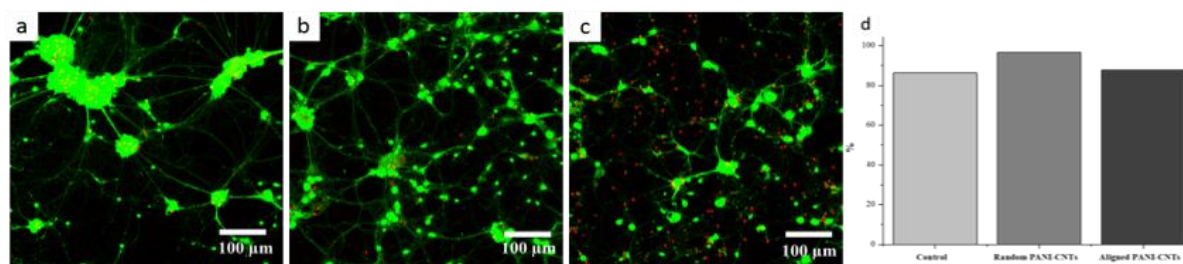

Figure 5. Live/Dead analysis of 2D cell culture. Confocal images of (A) pristine hydrogel, (B) randomly distributed PANI-CNTs/PAAm hydrogel, and (C) aligned PANI/3DCNW/PAAm hydrogel. (D) Cell viability graph of pristine hydrogel, randomly distributed PANI-CNTs/PAAm hydrogel, and aligned PANI/3DCNW/PAAm hydrogel.
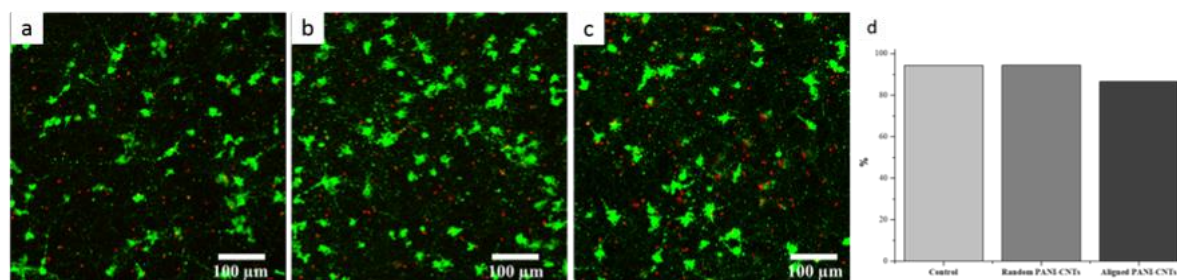
Figure 6. Live/Dead analysis of 3D cell culture. Confocal images of (A) pristine hydrogel, (B) randomly distributed PANI-CNTs/PAAm hydrogel, and (C) aligned PANI/3DCNW/PAAm hydrogel. (D) Cell viability graph of pristine hydrogel, randomly distributed PANI-CNTs/PAAm hydrogel, and aligned PANI/3DCNW/PAAm hydrogel.

Conclusions

As a result, we conclude that electrically conductive hydrogels composed of aligned PANI coated 3DCNW were biocompatible and permissible substrates for neural culture. However, we will discontinue the investigation of cell growth from the 2nd year of this project. We will rather focus on the detection of fluorescence-based antibody on modified surfaces for biosensor application.

1.2. Fabrication of 3DCNC structures and amine group functionalization with ammonia plasma

Introduction

CNTs have unique structural, chemical and electrical properties and those properties make them one of the promising materials for application in neuroscience. Our group has been working on the subject of CNT growth, channels, three-dimensional network, and their applications. Various 3D CNT structures were synthesized on several types of pillar templates by Chemical Vapor Deposition (CVD). We have developed a new "wall" style CNT structure which shows higher stability under strong acid condition and higher conductivity compared with 3DCNW. Meanwhile, benefit from acid treatment (which is a commonly used method for CNT functionalization) during the structure forming, CNT curtains are functionalized with carboxyl and hydroxyl groups. It also shows much better wettability compared with original CNT structure.

Experimental

Detailed CNT synthesis process has been explained in our previous works. The as-prepared sample was immersed into a mixed solution of H_2SO_4 (98%) and HNO_3 (60%) (Ratio= 3:1). After 12 hours, the sample was taken out and fully rinsed by DI water to remove acid residuals. Finally, the treated sample was dried at room temperature in atmosphere. The 3DCNW substrate was treated with NH_3/Ar plasma (50/70 sccm) at 50 W, 0.2 torr, 25°C using an inductive coupled

radio frequency PECVD for 15 min. SEM, Raman spectroscopy, XPS and contact angle measurement were carried out for characterization.

Results and Discussion

Figure 7 and Figure 8 show the SEM images of synthesized CNTs on pillar substrate and formed CNT micro-patterns after strong acid treatment, respectively. Vertically oriented CNTs are grown both on bottom and pillar surfaces with a height of ~ 7µm. Inset of Figure 7(b) shows the optical microscope image of CA on sample surface with a value of $150.3 \pm 2°$. CNT clusters grown on the pillar top surfaces make up a highly ordered micro-pattern which gives rise to a super hydrophobic surface property. Figure 8(a) shows the top view of formed CNT micro-patterns which is consisted of perfectly shaped and regularly ordered square CNT "well". Figure 8(b) 45° tilted view shows that densely packed CNTs formed very uniform CNT walls. Figure 8 (c) reveals the detailed morphology of formed CNT wall and CNTs are all densely aggregated on the pillar surface, and the inset in Figure 8(c) shows the contact angle of as formed CNT micro-patterns is $55.2 \pm 2°$. Different kind of 3D CNT curtain (3DCNC) structures have been successfully fabricated on other kinds of pillar substrates as shown in Figure 9.
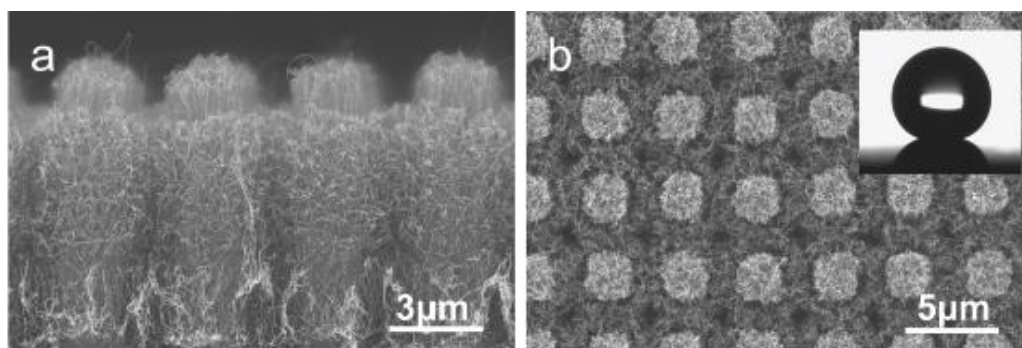

Figure 7. (a) Cross view and (b) top view SEM images of as synthesized CNTs on pillar substrate. Inset of (b) shows the optical microscope image of CA on sample surface with a value of $150.3 \pm 2°$.
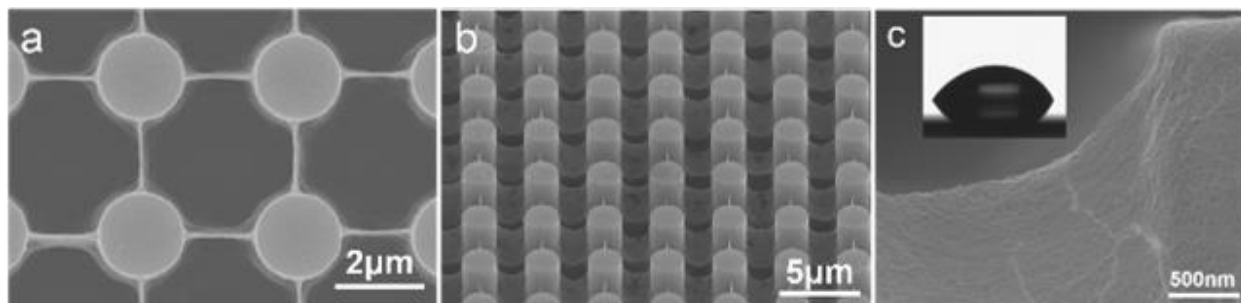

Figure 8. SEM images of formed micro-patterns after strong acid treatment: (a) top view of formed CNT micro-patterns; (b) 45° tilted view; (c) reveals the detailed morphology of formed CNT wall, the inset in (c) shows the contact angle of as formed CNT micro-patterns is $55.2 \pm 2°$.
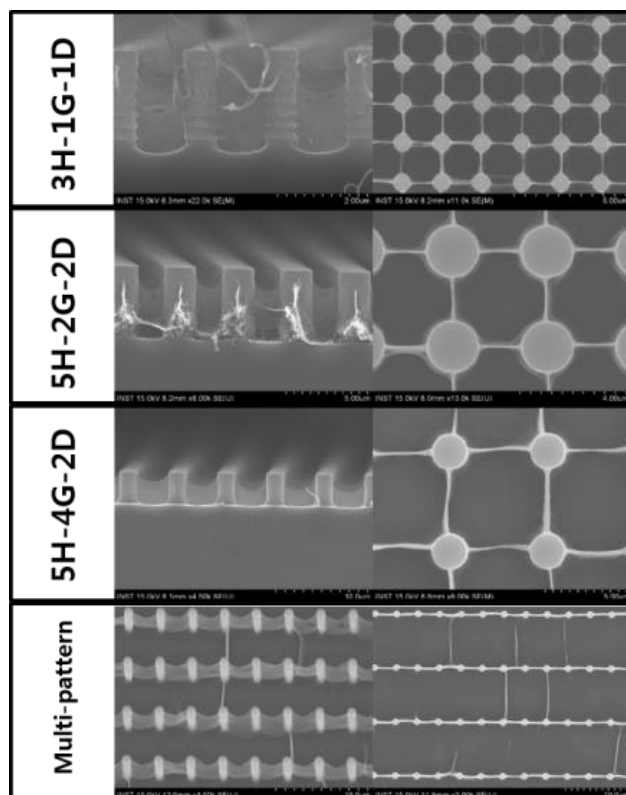
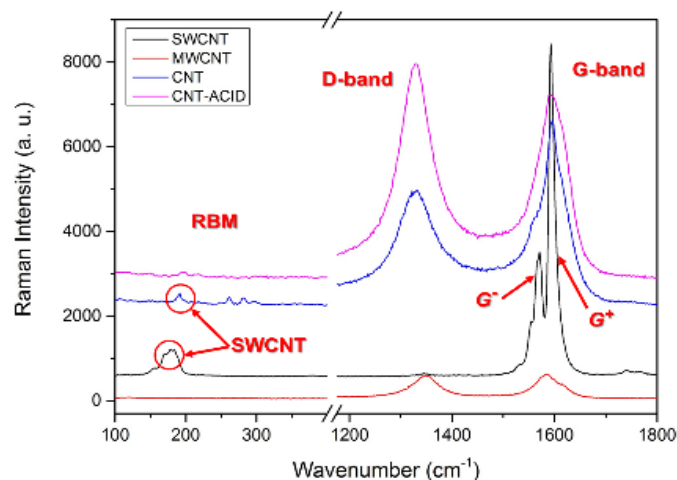Figure 9. 3D CNT curtain structures on different pillar substrates.

Figure 10. Different Raman spectra obtained from SWCNT, MWCNT, synthesized CNTs (CNT) and 3DCNC (CNT-ACID).

The structural properties of the as-prepared CNTs and 3DCNC were investigated by Raman spectra (Figure 10). Black spectrum and red spectrum are from pure single-walled carbon nanotube (SWCNT) and multi-walled carbon nanotube (MWCNT), respectively. Blue spectrum and purple spectrum are from the as synthesized CNTs and micro-patterned CNTs, respectively. RBM is detected in blue spectra which means SWCNTs appear. D band intensity is very high that means a lot of defects appeared. In addition, from the purple spectrum which collected from

the CNTs after acid treatment, we can see that RBM disappeared and G band becomes broader and smoother compared with the blue spectra. And the ratio of D/G is 1.16, which is doubled than the value 0.64 of blue spectrum. All the obvious changes from the Raman spectra indicated that small diameter SWCNTs were damaged or destroyed because of strong acid treatment, and more defects formed on CNTs.
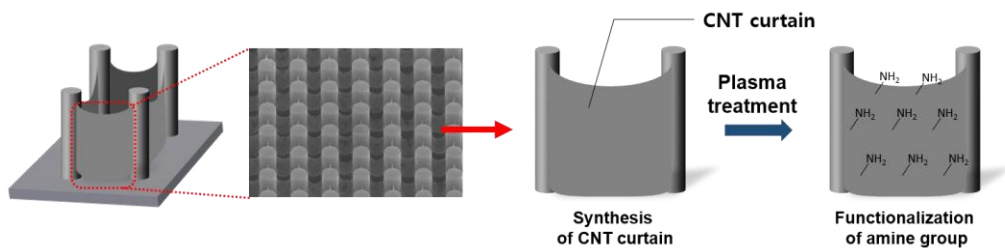
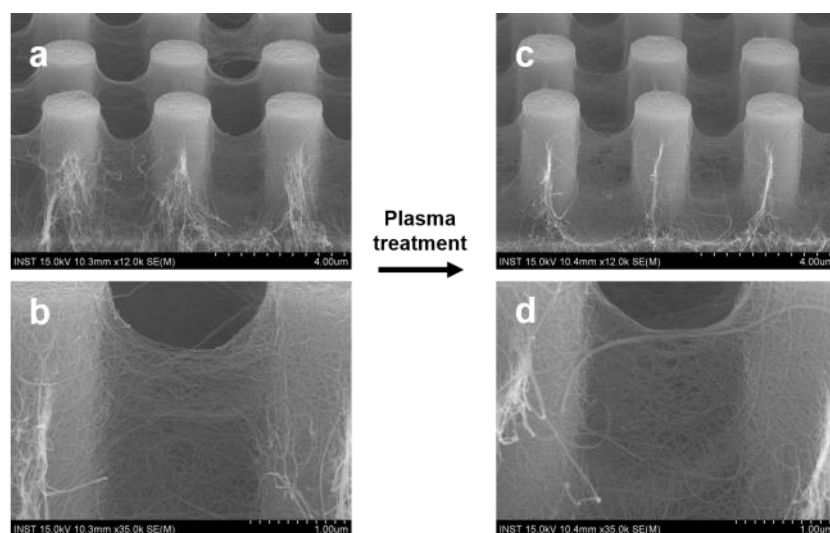Scheme 2. Amine group functionalization on CNT curtain by ammonia plasma treatment.

Figure 11. 3D CNT curtain structure before and after NH$_3$ plasma treatment.

Scheme 2 schematically illustrates the plasma treatment process on 3DCNC. After plasma treatment, the morphology of 3DCNC basically has no change and curtain structure are well sustained (Figure 11). To characterize the atom composition of the modified 3DCNC, XPS analysis was conducted (Figure 12). The treated 3DCNC is composed of not only carbon atom but also some oxygen atom and small amount of nitrogen atom. To acquire more information on the bonding structure of the 3DCNC after plasma treatment fitting spectra of C1s was analyzed. Figure 12b shows typical high resolution C1s spectra of the 3DCNC samples after NH$_3$/Ar plasma treatment for 15 min. The C1s spectrum is deconvoluted into five component Gaussian peaks: Peak (1) at 284.1 ± 0.2 eV, corresponds to the sp2-hybridized graphite-like carbon atom (C=C); Peak (2) at 285.1 ± 0.2 eV is attributed to the sp3 hybridized carbon atom (C–C); Peak (3) at 286.0 ± 0.2 eV is considered as C–O and C–N groups. Peak (4) at 287.2 ± 0.2 eV and peak (5) at 288.7 ± 0.2 eV are considered as C=O group and O–C=O group, respectively. Since the p bonds (C=C) in the sp2-hybridized graphite-like carbon within the CNT lattice are active and

chemical instability due to lack of rotation around C=C bonds and no saturation of C=C bonds, and therefore more susceptible to plasma attack. It is believed that radicals are first generated on the dissociated p bonds in C=C, which then further react with active NH radical. This process may produce C–NH, and then the C–NH$_2$ is quickly formed through stabilization by hydrogen atom transfer from the same or neighboring chain or plasma.
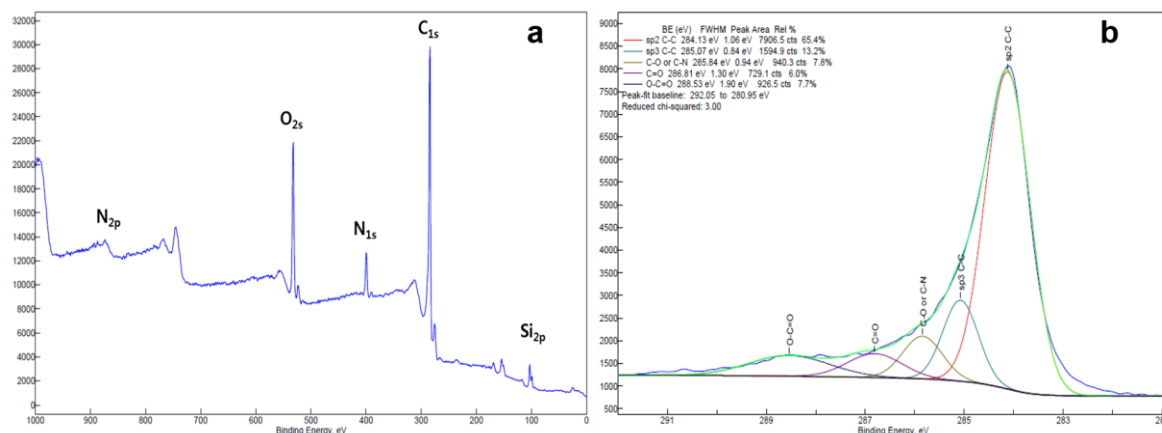

Figure 12. (a) XPS of plasma treated CNT curtain structure and (b) high resolution of C1s peak.

However, depending on those data above, the density of amino groups cannot be improved to achieve higher number of amine groups on the surface of CNT curtains. For confirming amine groups specifically, fluorescence-tagged biomolecules were conjugated onto the surface of 3DCNC, and very weak fluorescence signal was detected.

Conclusions

Although the surface of 3DCNC structure was modified under the NH$_3$/Ar plasma, an N1s peak was observed as emerging nitrogenous groups in XPS spectrum. The quantity of formed amino groups was not confirmed. More investigations will be carried out in the 2nd year.

1.3. Atomic layer deposition of Al$_2$O$_3$ and amine group generation on 3D CNT web

Introduction

3DCNW is the most often studied and used structure in PI's lab. However due to the pillar structure effect, CNTs between pillars are not stable enough under mild modification conditions while CNT surface modification is very necessary for biomolecule or biomaterials attaching. To apply this unique structure to bio area, another way to functionalize the 3DCNW surface was developed. Atomic layer deposition (ALD) method could be the best choice because target materials can be deposited on substrate surface layer by layer at atomic level and the thickness

could be well controlled. AEAPDMS self-assembly process is introduced to modify the CNT/Al_2O_3 surface with amino groups. For confirming amino groups, we introduce the conjugation of fluorescence-tagged biomolecules onto the surface of 3DCNW platform.

Experimental

ALD coating of Al2O3 on 3DCNW
Detailed 3DCNW synthesis process has been explain in our previous works. Synthesized 3DCNW was coated with Al_2O_3 for enhancing stability of 3DCNW into solution because the circumstance for biomarker detection normally performed into solution state. The thickness of Al_2O_3 layer were well controlled by deposition cycles. The morphology of 3DCNW and Al_2O_3-coated 3DCNW was measured by FE-SEM.

Surface modification and immobilization with anti-CA125 antibody
The surface modification of 3DCNW was important things for immobilization of biomolecules on the template. Amino groups on the surface of Al_2O_3-coated 3DCNW could be created by self-assembled monolayer method. Firstly, Al_2O_3-coated 3DCNW was treated with UV-O3 for 30 min in O_2 gas flow in order to remove organic contaminants and create hydroxyl group on the surface of Al_2O_3-coated 3DCNW on Si substrate. Secondly, the substrate was dipped into 1% AEAPDMS solution for 3hrs under nitrogen gas after UV-O3 treatment, and the amino-functionalized substrate was thoroughly washed with toluene and ethanol solution. In order to confirm amino group onto Al_2O_3-coated 3DCNW and possibility of sensor for detection of CA125 biomarker, Alexa488 tagged CA125 antibody as capture antibody was conjugated onto the amino-functionalized substrate through EDC-NHS crosslinking reaction. The capture antibody was prepared with the Alexa 488 protein labeling kit. Briefly, 5 μL of 1 mM EDC and 4 mM NHS added into 990 μL PBS (pH 7.4) containing various concentration of capture antibody ranged from 0.1 to 50 μg/mL and pre-reacted at 50 rpm for 15 min. The amino-functionalized substrate was located in 96 well plate and incubated into the crosslinking solution at 25°C for 3 hrs. After the reaction, the substrates were washed with washing solution (0.1% Tween20 in PBS) to remove excess reagent and non-binding capture antibody. The fluorescence microscopic images were taken from optical microscope. The fluorescence images were analyzed in ImageJ.

Results and Discussion

Figure 13a-c showed the CNTs between pillars on Si substrate after synthesis of CNTs under C_2H_2 gas using LPCVD for 20 min. The most of CNTs were formed between the neighboring pillars but less CNTs was frequently interconnected between diagonal pillars. The CNTs were known to be aggregated into hydrophilic and hydrophobic solution due to van der waals interaction or adhesion force between adjacent CNTs. And thus, the hierarchical CNTs structure of 3DCNW was collapsed even destroyed during modification processes. Figure 13d-f showed the SEM image of 3DCNW after 15 nm Al_2O_3 coating. The diameter of the Al_2O_3 coated CNT

bundle was about 45-50 nm. The morphology of 3DCNW after Al_2O_3 coating was well maintained during surface modification steps.
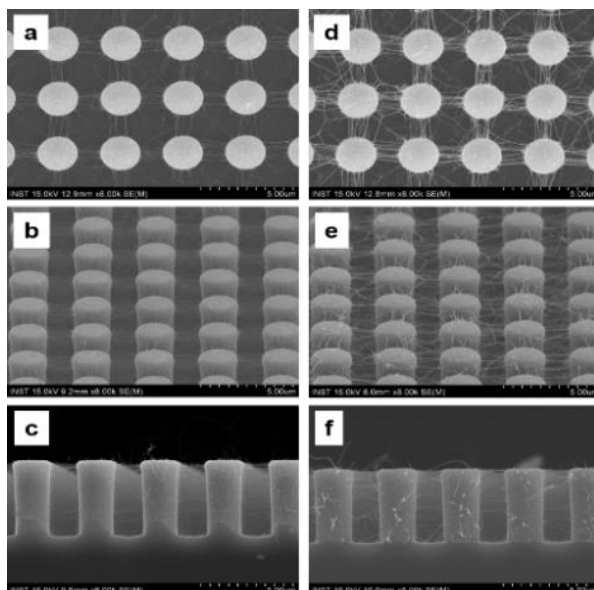

Figure 13. The SEM images of 3DCNW (a,b,c) and after atomic layer deposition(d,e,f). (a, d) Top view, (b, e) tilt view and (c, f) side view.

EDC/NHS reaction is well known to bioconjugation technique which is crosslink primary amines to carboxylic acid groups using EDC/NHS. In order to confirm the amino group on the surface of 3DCNW, fluorescence isothiocyanate (FITC) tagged-antibody is bonded on the amino-functionalized 3DCNW using EDC/NHS reaction. Scheme 3 schematically illustrates the fluorescence intensity for seven different concentration of FITC-antibody conjugated on amino functionalized 3DCNW. As shown in Figure 14, fluorescence signal could obtain from 1 μg/mL of FITC-tagged antibody conjugated on 3DCNW and enhanced signal with increasing concentration of the antibody up to 10 μg/mL. This result indicated that AEAPDMS coated 3DCNW has successfully formed amino groups on the surface, and amino functionalized 3DCNW is easily modified with peptide, protein, and antibody through bio-conjugation steps.
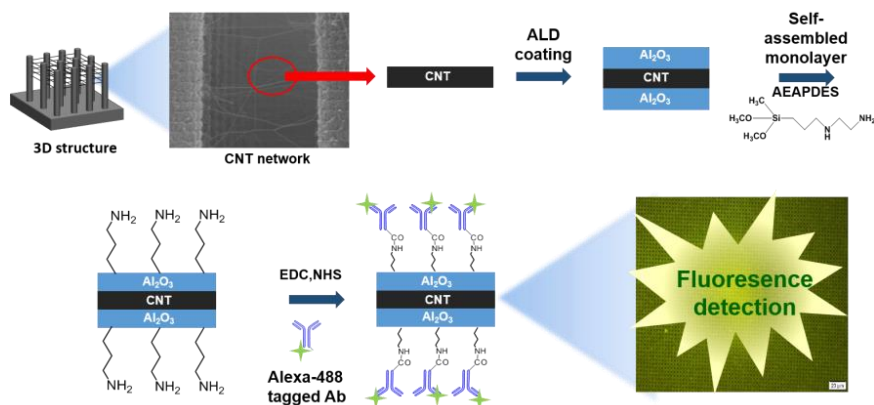
Scheme 3. Schematic illustration of fluorescence-based biomolecules conjugation on the surface 3DCNW for amino groups' confirmation.
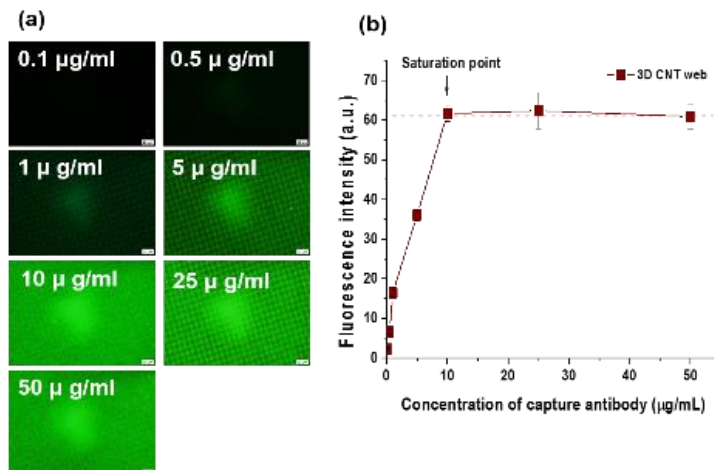
Figure 14. (a)The fluorescence images and (b) the fluorescence intensity for seven different concentration of FITC-antibody conjugated on amino functionalized 3DCNW.

Conclusions

Al_2O_3 layer deposited by ALD on 3DCNW surface was well sustained in the web structure, and it provides a stable surface for amino group modification. The surface onto Al_2O_3 coated 3DCNW was modified by AEAPDMS SAM and we confirmed amine modified surface onto the template through bio-conjugation step using fluorescence-based antibody. The results indicated that amino groups are well modified on the 3DCNW surfaces and it could be applied to biosensor.

1.4. Amine group functionalization of 3DCNW by C_2H_2 and NH_3 plasma treatment

Introduction

For 3DCNW structure, although we could modify the CNTs by NH_3 plasma treatment as we mention in part 1.2, the low density of CNTs in 3DCNW hinders the modification process as CNTs could be all etched out by plasma etching effect. Hence, another way to strengthen the CNT stability was developed by introducing a pretreatment with C_2H_2 plasma before NH_3 plasma treatment step. Fluorescence signals are detected by binding FITC on the amine-functionalized 3DCNW.

Experimental

The 3DCNW substrate was treated with C_2H_2 plasma (100 sccm) at 50 W, 0.11 torr, 25°C using PECVD for 5 min. The atomic ratio of the 3DCNW was determined by XPS analysis. Subsequently, C_2H_2 pre-treated 3DCNW was treated with NH3 plasma (20 sccm) at 100 W, 0.11 torr, 25°C using PECVD for 80 min. Exposed amine groups on 3D-CNTs were evaluated using FITC conjugation. 100 µg/mL of FITC was dissolved in acetone and C_2H_2/NH_3 plasma treated 3DCNW was immersed into FITC solution for 1 hr. The 3DCNW was washed 5 times with DI water and observed fluorescence signal by using fluorescence microscope.
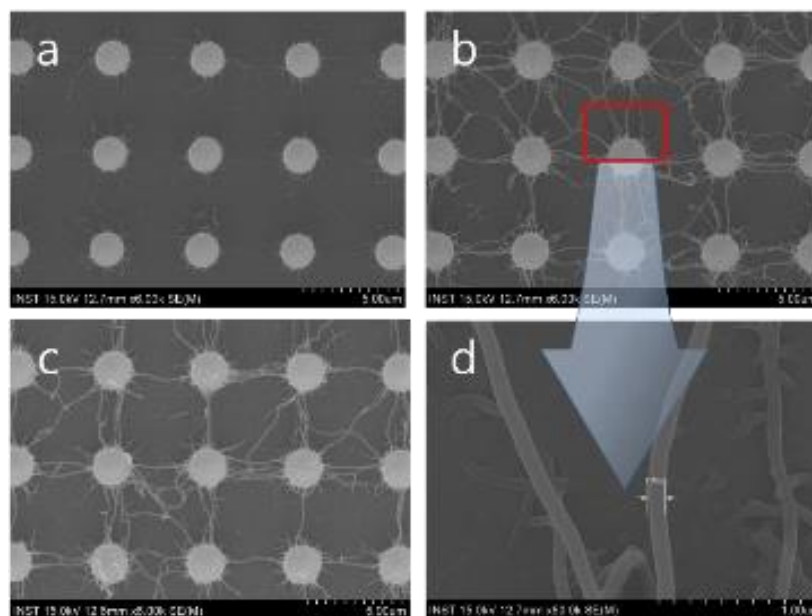
Results and Discussion

Figure 15. The SEM images of (a) pure 3DCNW, (b) C_2H_2 plasma treated 3DCNW, (c) C_2H_2/NH_3 plasma treated 3DCNW and (d) C_2H_2 plasma treated 3DCNW (magnification 50 K).

Figure 15 showed (a) 3DCNW, (b) C_2H_2 plasma treated 3DCNW and (c) C_2H_2/NH_3 plasma treated 3DCNW. The CNTs were synthesized between pillar Si substrate and its morphology has several types of shape such as straight, arch and double y-junction. The thickness of CNT bundle was approximately 10-20 nm. The thickness of CNT in 3DCNW after treatment of C_2H_2 plasma was about 100-120 nm and it is 6 times more increase than CNT bundle. In order to amine functionalize the surface of C_2H_2 treated 3DCNW, the 3DCNW was re-treated with NH_3 plasma. As shown in figure 16, pure 3DCNW and NH_3 plasma treated 3DCNW was not observed with green fluorescence signal. Fluorescence images of C_2H_2 plasma treated 3DCNW slightly increased the signal but it showed background signal. In contrast, fluorescence signal of C_2H_2/NH_3 plasma treated 3DCNW was significantly increase. These results suggested that C_2H_2/NH_3 plasma treated 3DCNW was successfully functionalized amine groups on the surface.
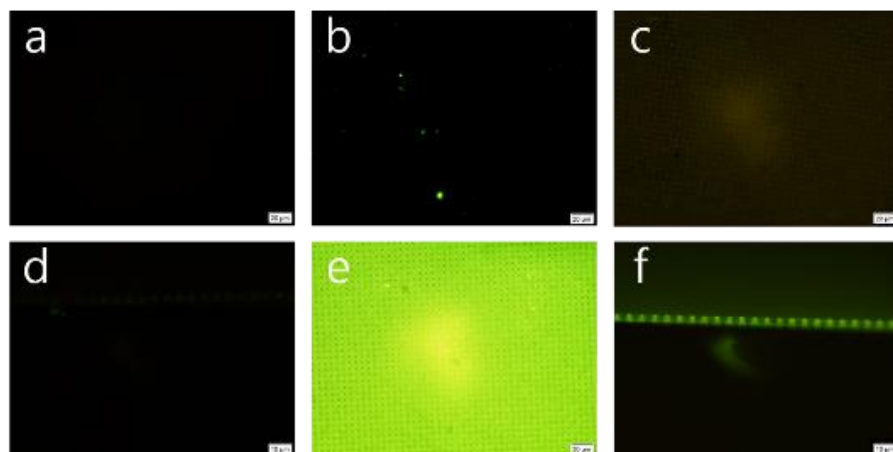
Figure 16. (a) CNT (b) NH$_3$ plasma treated 3DCNW, (c) C$_2$H$_2$ plasma treated 3DCNW (top) (d) C$_2$H$_2$ plasma treated 3DCNW (side) (e) NH$_3$ plasma treatment of C$_2$H$_2$ plasma treated 3DCNW (f) NH$_3$ plasma treatment of C$_2$H$_2$ plasma treated 3DCNW.

Conclusions

C$_2$H$_2$ plasma pretreatment followed by NH$_3$ plasma treatment is an efficient way to modify the 3DCNW with amine groups. However, the mechanism of this modification method needs to be confirmed during our following works.

2. Second Year Progress

In the 1st year, electrically conductive hydrogels composed of polyaniline coated 3DCNW in 1D direction were prepared as biocompatible substrates for biomolecule culture. However, the proposed research did not go through well because the biomolecules were not cultured without significant directionality under the applied potential. From the 2nd year, PI had to change the themes of proposed research and we have started the investigation of three-dimensional carbon nanotube web structures (3DCNW) as a potential biosensor platform owing to its large surface area for improving sensing capability. Fluorescence-based immunoassay using 3DCNW showed a quantitative detection of Cyfra 21-1 antigen (OSCC biomarker) and its limit of detection is 10 times lower than that of conventional ELISA method. It seems that there are some limitations to be implemented for practical use such as expensive fabrication cost and long surface modification processes as a biosensor platform. To overcome these limitations, we have been developing noble polygon-shaped CNT wall structures on Si substrates with a simple approach, which are rather easily generated from vertically grown CNT forest by a solvent-assisted deformation process. In order to employ this process for the preparation of a biosensor platform, the surface of CNT walls was successfully modified by RF plasma treatment. The characteristics of biomarker detection using both CNT wall structures and 3DCNW are optimistic. However, in consideration of process conditions and cost effectiveness we believe that the template fabricated with CNT wall structures should be better one. For exploring CNT-based biosensor or CNT-embedded strain sensor in flexible devices, our team is currently developing a new platform in which a noble CNT wall structure is gently embedded onto the upper part of PDMS film. We have confirmed that the surface of CNT wall structure on PDMS film can be well functionalized with amine groups under the various optimum conditions of RF-plasma treatment. In the next year, our team will present the outcome and impact of a CNT wall structure based PDMS film as a highly sensitive and cost-effective flexible sensor.

2.1. Fluorescence-based immunosensor using three-dimensional CNT network structure for sensitive and reproducible detection of oral squamous cell carcinoma biomarker

OSCC is the most common cancer of the oral cavity and the leading cause of death in the developing countries, and the mortality rate of OSCC patients has not significantly changed in the past 30 years. Early detection of OSCC is a critical issue for the long-term survival of patients and successful treatment of cancer. Histopathological examination and biopsy have been used for a long time as a representative method of OSCC diagnosis. However, these processes are slow and time-consuming as well as critical diagnosis requires the professional interpretation by experienced pathologists if cellular or molecular changes were detected. According to advances in molecular biology, clinical evaluation using cancer biomarker is considered to be useful for early diagnosis and prognostic monitoring with histopathological examination. Cancer biomarkers such as antigens, DNA, mRNA and enzymes are an important indicator for staging the pathological progression of the disease, and protein markers are most commonly used for cancer diagnosis. The level of several biomarkers such as carcinoembryonic antigen, squamous

cell carcinoma, immunosuppressive acidic protein and cytokeratin 19 fragment (Cyfra 21-1) in blood sample of OSCC patients led to sensitive and accurate diagnosis. In recent decades, salivary analysis for OSCC diagnosis has become an alternative tool to the serum testing because saliva collection is simple, safe, painless, and non-traumatic and can be taken repeatedly.

Immunoassay-based methods have been widely used to deter- mine the biomarkers in tumor tissues and body fluids such as blood, saliva and urine. Several types of immunoassay such as enzyme-linked immunosorbent assay (ELISA), fluorescence-based immunoassay, electrochemical sensor, chemiluminescence immunoassay, and multiplexed bead platforms have been explored for diagnostics of disease. An analysis of the current state of the art reveals an unmet medical need in the management of oral carcinoma. Thus, novel strategies have been extensively worked out in the context of analytical platforms as well as diagnostic tools for rapid, sensitive and reproducible detection of biomarkers.

Materials and methods

Fabrication of 3DCNWs
The fabrication of 3DCNWs was carried out as described in the previous reports. The deposition of Al_2O_3 onto 3DCNWs was conducted for 150 cycles by using ALD. The morphology of 3DCNWs and Al_2O_3-coated 3DCNWs was examined by FE-SEM and Raman spectroscopy.

Amine functionalization of Al2O3-coated 3DCNWs
Al_2O_3-coated 3DCNWs were functionalized with amine groups by self-assembly process of AEAPDMS for antibody immobilization. Briefly, the Al_2O_3-coated 3DCNWs were exposed to ultraviolet (UV)-activated oxygen in a UV-ozone chamber for 30 min to remove organic contaminants and generate hydroxyl groups on the surface of Al2O3. **They were d**ipped into 1% AEAPDMS solution for 3 h under nitrogen atmosphere followed by washing with non-hydrous toluene and absolute ethanol thoroughly. In order to confirm the formation of monolayer on the surface of templates after SAM modification, Al_2O_3-coated 2D Si substrates were also modified with the same procedures described above. The surface morphology of Al_2O_3-coated 2D Si substrates after SAM modification was identified by atomic force microscope (AFM), and the thickness of self-assembled aminosilane layer was measured by ellipsometer. The amino group after SAM modification initiated by the imine formation reaction between 4-nitrobenzaldehyde and amine group dated using a UV/Vis/NIR spectrometer as described in the previous report. The number of amino groups was calculated through Beer-Lambert equation using individual absorbance of 4-nitrobenzaldehyde (at lmax 267 nm) after hydrolysis of 4-nitrobenzaldehyde conjugated each 2D Si substrate and 3DCNWs.

Determination of pair antibodies against Cyfra 21-1
The binding assay was performed on BLItz system in order to identify the binding selectivity of paired antibodies against Cyfra 21-1. Prior to binding measurements, Anti-mouse IgG Fc Capture (AMC) biosensor was equilibrated for 10 min in PBS. After an initial baseline for 30 s, capture antibody was loaded onto the AMC-coated sensor for 120 s. The biosensor was washed for 30 s

by flowing through PBS and Cyfra 21-1 was then associated with for 120 s, followed by washing for another 30 s in PBS. The detection antibody was associated with for 120 s, followed by dissociation for 120 s in PBS. Pair antibodies were identified as suitable for assay development using a BLItz Pro software.

Quantification of Cyfra 21-1 with 3DCNWs sensor
Capture antibody was immobilized onto the amine-functionalized Al2O3-coated 3DCNWs by EDC-NHS crosslinking reaction. Each 5 mL of 1 mM EDC and 4 mM NHS was added into 990 mL PBS (pH 7.4) containing 10 mg capture antibody for pre-reaction at room temperature for 15min. The amine- functionalized Al_2O_3-coated 3DCNWs were placed in a 96 well plate and incubated in the 100 mL of antibody solution at 25 C for 3h. After the reaction, the 3DCNWs were washed with 0.1% Tween 20 in PBS (T-PBS) thoroughly to remove any excess reagents and non-binding capture antibodies. Capture antibody-immobilized 3DCNWs were incubated at 100mL of eleven different concentration of Cyfra 21-1 in the range from 0.1 to 10,000 ng/mL for 1 h, subsequently washed with T-PBS to remove unbound biomarkers. Next, each 3DCNWs was incubated in 100 mL of 10 mg/mL of Alexa 568-tagged detection antibody solution for 1 h and then non-binding antibodies were washed out. The fluorescence microscope images of 3DCNWs at different concentrations of Cyfra 21-1 were obtained using a BX51W1 upright fluorescence microscope with a 50-objective lens at an exposure time of 500 ms. The fluorescence images were analyzed with ImageJ software. In order to compare the sensitivity of 3DCNWs, the sandwich ELISA was employed at the above-mentioned concentrations of Cyfra 21-1 according to the general procedure suggested for sandwich ELISA.

Assays of clinical saliva samples
The Cyfra 21-1 in clinical saliva samples were analyzed to assess the diagnostic feasibility and capability of fluorescence-based 3DCNW immunoassay method. The 11 saliva samples were collected from 4 healthy persons and 7 OSCC patients at the Department of Oral and Maxillofacial Surgery, Korea University Hospital. The clinical study was approved by the Institutional Review Board (IRB) at the hospital. Consent documents were also obtained from all patients included in this study.

The saliva samples were centrifuged at 12,000 g for 5 min, and the supernatants were passed through a 0.45 mm pore-sized syringe filter. The clear supernatants were aliquoted and frozen for storage at 80 °C until thawed for analysis. All experiments were performed within 2 weeks after sampling. The samples were thawed in room temperature until completely thawed. Non-diluted clinical samples were assayed using a commercially available ECL assay system. The clinical samples were diluted two-fold with PBS buffer for the assay of the 3DCNWs sensor and the results were compared with those determined by the ECL assay method.

Results and Discussion

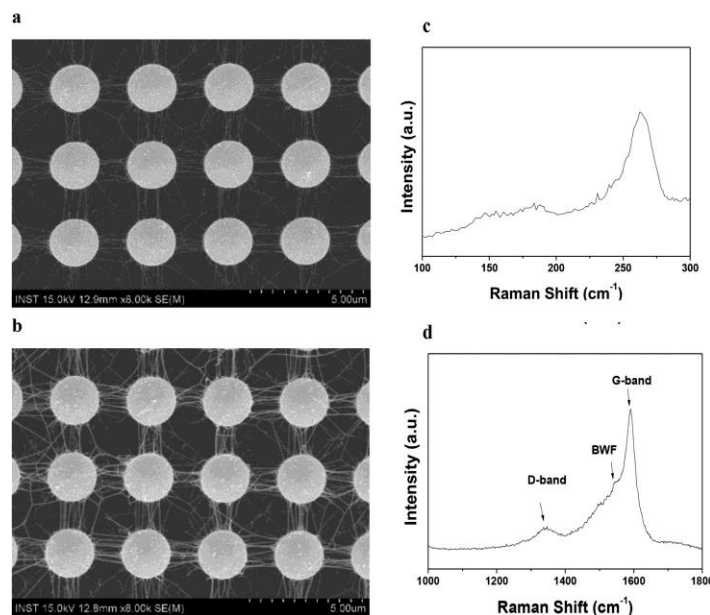**Structural properties and stabilization of 3DCNWs**

Figure 17. The SEM images of (a) 3DCNWs and (b) 3DCNWs after ALD coating with Al_2O_3. (c) and (d) Raman spectra of 3DCNWs are an enlarged view of the RBM frequency range and the G/D frequency range, respectively. The wavelength of the excitation lasers is 514.5 nm.

The hierarchical CNT networks on Si substrates prepared as a sensor template to increase the sensitivity of biomarker measurement. As shown in Figure 17a, CNTs were synthesized on Si pillar- patterned substrates and interconnected in a hierarchical shape between adjacent pillars. The interconnected CNTs between pillars were observed in various shapes such as straight, arch and double Y-junction between pillars and the mean diameter of single CNTs bundles connected between pillars was about 10~15 nm. The Raman spectra showed that the synthesized CNTs were composed of SWCNTs assembled in a bundled structure and the diameter of SWCNTs was calculated to be about 0.9 nm as reported previously (Figure 17c and 17d).

The hierarchical morphology of CNTs between adjacent pillars was aggregated due to Van der Waals interaction and capillary force between adjacent CNTs during solution drying process. Thin aluminum oxide layer was grown on the surface of 3DCNWs by ALD technique in order to achieve mechanical and structural stability of the hierarchical CNT networks. Figure 17b showed the morphology of 3DCNWs after Al_2O_3 coating and the diameter of CNT bundle coated with Al_2O_3 was estimated to be 35 ± 5 nm. The hierarchical morphology of 3DCNWs was well maintained in aqueous solutions during the surface modification, immobilization processes or biomarker assay after Al_2O_3 coating. These results indicated that Al_2O_3-coated 3DCNWs can be utilized as a template for biomolecule recognition under solution phases.
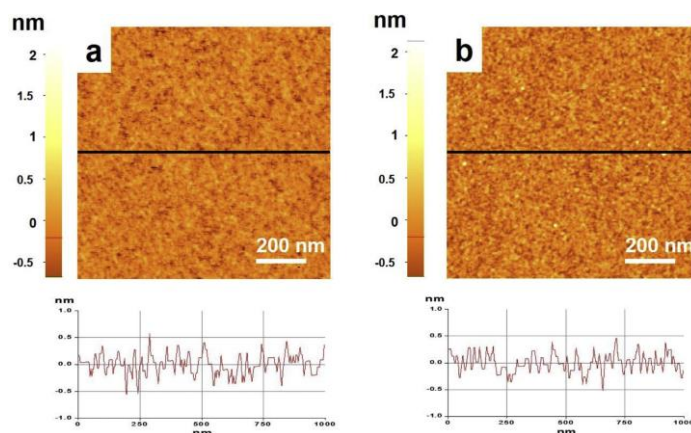
Figure 18. Non-contact mode AFM images (top) and cross-sectional profiles (bottom) of (a) Al$_2$O$_3$-coated 2D Si substrate and (b) Al$_2$O$_3$-coated 2D Si substrate after SAM modification (3 h). The scan size is 1.0 mm*1.0 mm. The RMS roughness is about 0.185 nm for (a) and (b).

Surface functionalized template for antibody immobilization

AEAPDMS was chosen to generate monolayer formation and amine functionalization on the surface of templates for uniform immobilization of antibody on the Al$_2$O$_3$-coated 3DCNWs. The surface properties of Al$_2$O$_3$-coated 2D Si substrate after SAM modification were characterized by using ellipsometer and AFM. The measured thickness of aminosilane layer on a Si substrate after 3 h of SAM modification was 11 ± 1 Å which was close to the theoretical thickness of AEAPDMS monolayer. Figure 18a and b showed 1.0 mm×1.0 mm AFM images of Al$_2$O$_3$-coated 2D Si substrate and AEAPDMS modified Al$_2$O$_3$-coated 2D Si substrate after SAM modification, respectively. Non-contact mode AFM images did not show any aggregated multilayer formation after SAM modification. The RMS value of Al$_2$O$_3$-coated 2D Si substrate was 0.186 nm and it was similar to RMS values after SAM modification. The amine group on the surface after SAM was characterized by imine formation reaction between the amine group and 4-nitrobenzaldehyde. The absorbance values of 4-nitrobenzaldehyde at aminosilanized 2D Si substrate and 3DCNWs were converted into 0.89 and 2.40 of the amine groups in 100 Å, respectively. The absolute amine density of 3DCNWs after SAM modification was about 2.70 times higher than that of 2D Si substrate. On the basis of these results, the resultant layer on 3DCNWs after SAM modification was regarded as quasi-monolayer with successfully functionalized amine groups on the surface. The uniform modification of 3DCNWs can offer the reproducibility of antibody layer after immobilization of antibody.

Quantitative analysis of Cyfra 21-1 using 3DCNWs sensor

Scheme 4 illustrated the fluorescence-based immunoassay using 3DCNWs for the quantitative analysis of Cyfra 21-1. Paired antibodies against Cyfra 21-1 were selected by the binding assay using BLItz system which measures the shift in the interference pattern of the reflected light between the biomolecule-binding layer and an internal reference layer on a disposable fiber optic- based surface (Figure 19). Various concentrations of Cyfra 21-1 in PBS solution were captured on the surface of 3DCNWs through antibody-antigen interaction, and Alexa-fluor 568-tagged anti- bodies were formed sandwich immunocomplexes. Figure 20a showed that the fluorescence intensity was significantly enhanced with increasing concentrations of Cyfra 21-1
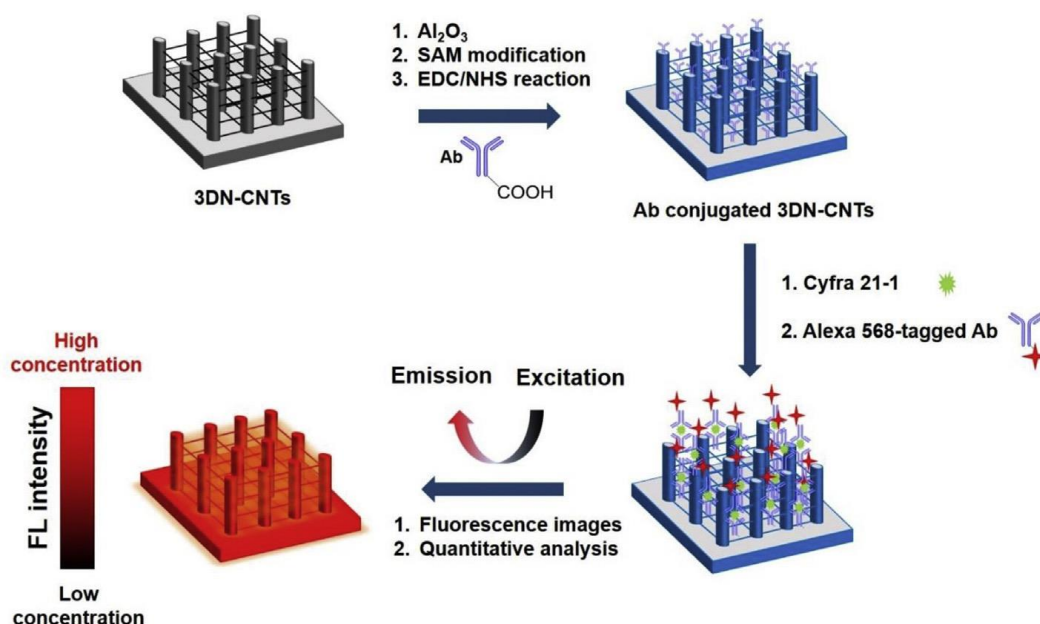
Scheme 4. Schematic illustration of the 3DCNWs sensor for Cyfra 21-1 detection.

in the range from 1 to 1000 ng/mL. The fluorescence intensity values on each fluorescence image were converted into fluorescence enhancement ratio (F/F0) and then plotted on a calibration curve with log scale of concentration (x-axis). As shown in Figure 20b, the calibration curve is the sigmoidal in shape ranged from 0.1 to 10,000 ng/mL and the calibration curve was used for quantitative estimation of Cyfra 21-1 by 4-parameter logistic (4-PL) model for curve-fitting analysis . The adjusted R-squared of the experimental data according to 4-PL model is 0.993. The limit of detection (LOD) of Cyfra 21-1 measured by 3DCNWs sensor was found to be 0.5ng/mL and it was determined by 3.3 times higher than the standard deviation of blank. The precision of the 3DCNWs sensor was evaluated by repeatedly assaying using coefficients of variation (CVs, n 1⁄4 3). As shown in Table 1, the 3DCNWs sensor above LOD was shown to be with a CVs below 10%, and the CVs of 3DCNWs sensors at 1e1000 ng/mL of Cyfra 21-1 was 2.38e8.60%. The CVs results range from 1 to 1000 ng/mL were shown in reliable reproducibility for Cyfra 21-1 measured by 3DCNWs sensor. In addition, the sensitivity of 3DCNWs sensor was compared with a conventional ELISA method using same pair antibodies and antigen. The sensitivity of 3DCNWs sensor was approximately 20 times higher than that of the sandwich ELISA (Figure 20c). The sensitivity enhancement of 3DCNWs sensor could be caused by increasing the maximum number of capture antibody on the surface because the total binding sites of 3DCNWs were estimated about three times higher than that of 2D Si substrate. In addition, the hierarchical structure of 3DCNWs increases the accessibility of biomolecules through the ordered pathways of 3DCNWs templates.

For clinical trials, the performance of 3DCNWs sensor in saliva samples (4 healthy persons and 7 OSCC patients) was compared with that of a commercially available ECL assay system. The ECL assay data of healthy persons (sample 1 to 4) were estimated at ranged from 2.6 to 4 ng/mL and those of OSCC patients (samples 5 to 11) were estimated at ranged from 4.2 to 62.5ng/mL The quantitative estimation of Cyfra 21-1 in saliva samples measured by 3DCNWs sensor was

consistent with those of ECL assay within clinical range. Table 1 showed that the analytical precision of 3DN- CNTs sensors in clinical samples was evaluated by the CVs, and the Mean CV
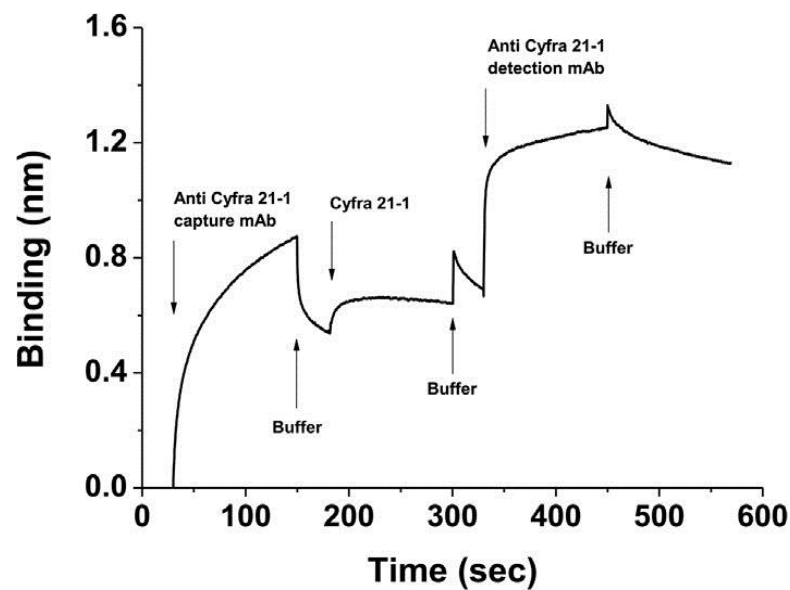

Figure 19. Bio-layer interferometer binding analysis of pair antibodies against Cyfra 21-1.
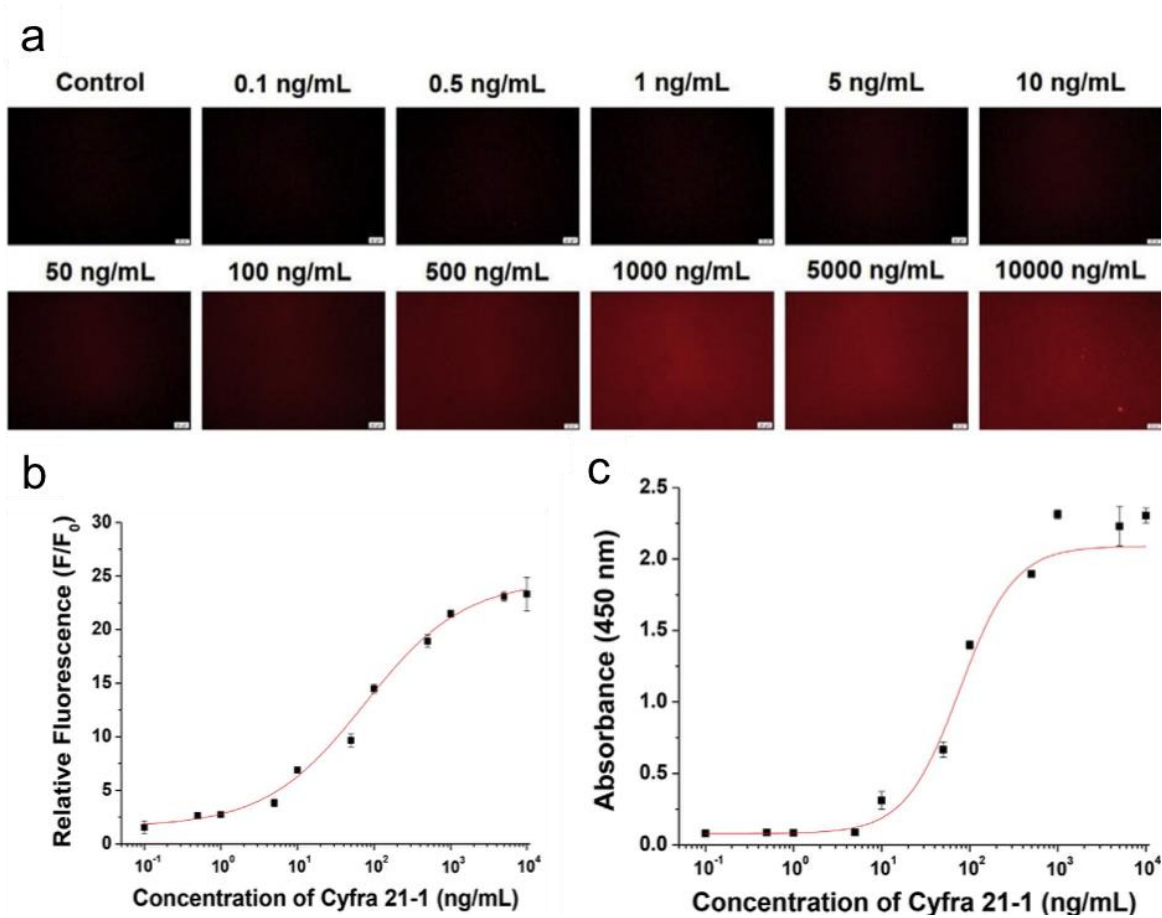
Figure 20. Representative fluorescence images of (a) 3DCNWs sensor at different con- centrations of Cyfra 21-1. (b) The calibration curve for Cyfra 21-1 on 3DCNWs sensor. (c) The standard calibration curve from a conventional sandwich ELISA.

was estimated to be 11.92%. The similarity of two analytical methods was performed with Passing and Bablok regression analysis for 3DCNWs sensors versus ECL assay. The statistical procedure is a suitable non-parametric regression anal- ysis and allows estimation of variation and systematic for comparative studies between two different analytical methods. Figure 21 showed no significant deviation from linearity (Cusum test for linearity; P 1⁄4 0.77) and scatter point (black circle) and regression line (blue) of the results were included within 95% confidence intervals (CIs). These results indicated that two different analytical methods had good conformity and were valid for clinical saliva samples in the range from 1 to 62.5 ng/mL. As demonstrated herein, 3DCNWs biosensor could be proposed as a complementary sensor for the ECL assay with the limitation of quantitative analysis of some biological materials caused by a quenching effect.
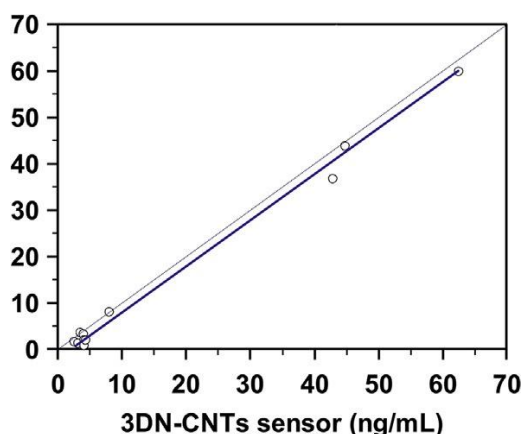
Figure 21. Passing and Bablok regression analysis (a) between 3DCNWs sensor and ECL assay.

Table 1. The mean value, SD, and CVs of fluorescence enhancement ratio (F/F0) according to Cyfra 21-1 concentration measured by the 3DCNWs sensor.

Cyfra 21-1 (ng/mL)	Fluorescence enhancement ratio (F/F$_0$)		
	Mean value	Standard deviation	CVs, %
0.1	1.54	0.58	37.55
0.5	2.64	0.19	7.07
1	2.76	0.11	4.12
5	3.85	0.26	6.11
10	6.52	0.44	6.79
50	9.09	0.74	8.18
100	13.88	0.98	7.03
500	18.96	0.45	2.38
1000	23.28	2.00	8.60
5000	24.56	1.65	6.70
10,000	24.98	2.27	9.07

※ CVs: coefficient of variations.

Conclusions

Sensitive and reproducible 3DCNWs sensor was prepared for the detection of Cyfra 21-1 as OSCC biomarker. The surface of Al_2O_3-coated 3DCNWs was uniformly modified with amine groups for facilitating antibody immobilization. Potential application 3DCNWs as fluorescence-based immunosensor was investigated through quantitative analysis of Cyfra 21-1. The LOD of the 3DCNWs sensor was estimated to be 0.5 ng/mL and the calibration curve of Cyfra 21-1 was sigmoidal in shape ranged from 0.1 to 10,000 ng/mL with r square 1/4 0.993. The sensitivity of 3DCNWs sensor was approximately 20 times higher than that of the conventional sandwich ELISA system. The 3DCNWs sensor improved the detection sensitivity of Cyfra 21-1 because of unique structural properties such as increase of total binding sites, hierarchical structures for the easy accessibility of biomolecules. The results of Cyfra 21-1 in saliva samples measured by 3DCNWs sensor showed a linear relationship and good conformity with those measured by ECL assay, and the mean CVs values of 3DCNWs sensors were less than 15% (CV cut-off value). The 3DCNWs could be used as a feasible biosensor for diagnosis of OSCC in clinical saliva samples.

2.2. CNT wall and CNT wall/PDMS structures

Introduction

The polygon-shaped CNT wall structures on a Si substrate was investigated with a simple approach, which are rather easily generated from vertically grown CNT forest by a solvent-assisted deformation process. In order to employ this process for the preparation of a biosensor platform, the surface of CNT walls was successfully modified by RF plasma treatment. The characteristics of biomarker detection using both CNT wall structures and 3DCNW are optimistic. A template fabricated with CNT wall structures is more effective and better to use for biomarker detection.

For exploring CNT-based biosensor or CNT-embedded strain sensor in flexible devices, a new platform in which a noble CNT wall structure is gently embedded onto the upper part of PDMS film. It is confirmed that the surface of CNT wall structures on PDMS film was functionalized with amine groups under the various conditions of RF-plasma treatment and the density of amine groups is controlled. CNT wall structures embedded PDMS film is promising as a sensitive and cost-effective flexible sensor.

Experiments

Synthesis of vertically grown CNTs (V-CNTs)
Cleaned Si wafer was dipped into the bi-catalyst solution for two hours, shortly thereafter, it was taken out and directly blew using nitrogen gun. Vertically multi-walled CNTs were grown on the deposited Fe-Mo catalyst Si substrate by means of LP-TCVD method. The catalyst deposited Si substrate was placed in the center of the reactor and the reactor was pumped down to a pressure lower than 1×10^{-2} torr with ramping temperature. When the temperature was reached 720°C, 200 sccm of H_2 gas flowed into the reactor for 10 min as

reduction process of the iron oxide converted into the iron catalyst at 2.9 torr. After that, 100 sccm of C_2H_2 gas flowed for 6 min with a pressure of 1.3 torr to synthesize the V- CNTs.

Fabrication of H-CNT/PDMS composites
The synthesized V-CNTs were immersed in the acetone at ambient condition for 10 min and followed by acetone evaporation in a vacuum chamber at $3\times10-2$ torr pressure for 1 hour to generate H-CNTs which formed by capillary-driven force self-assembly and Van der Waals force as shown in Scheme 5. As shown in Scheme 6, the H-CNT/PDMS composites were fabricated by pouring the prepolymer PDMS on the molding template and followed by attaching the reversed H-CNTs on the prepolymer PDMS, then degassed for 1 hour in a desiccator. After degassing process, it was cured at 80℃ for 1 hour and cooled down until reach the room temperature. The silicon substrate of H-CNTs was removed and peeled off the H-CNT/PDMS composites from the molding template. The resultants H-CNT/PDMS composites have a thickness around 600 μm and were cut into 3 x 1 cm^2 in size.

Surface modification of CNTs by plasma treatment
For the modification of the CNTs surface using PECVD methods, the synthesized 3D network of CNTs was placed in the PECVD chamber. When pressure condition was reached at below 5.0 x 10-6 torr, the plasma treatment was carried out at 0.05 torr, 50 W, at room temperature for 5 min. After the plasma treatment, reactive gas was removed at the vacuum state for 10 min. Ammonia gas plasma treatment of surface follows the similar process as mentioned above. C_2H_2 pre-treated CNTs were treated with NH_3 (20 sccm) plasma at 100 W, 0.11 torr, ambient temperature using PECVD for 80 min to confirm the amino groups. After the plasma treatment, reactive gas was removed at the vacuum state for 10 min.

Morphological Analysis
The V-CNTs, H-CNTs and CNT/PDMS composites were examined by FE-SEM. The height and diameter of V-CNTs and H-CNTs were compared by looking at SEM images. The surface morphology of H-CNT/PDMS composite strain sensor was also characterized by using SEM

Raman Spectroscopy Analysis
Raman spectroscopy was used to investigate whether there are a damaging CNTs or not. Raman spectroscopy analysis was performed using a WITec UHTS Raman Spectrometer with a laser excitation wavelength of 532 nm at identical laser powers of 50 mW. Generally, the CNT Raman spectra provide useful information such as diameter, chirality, structural quality, metallic or semiconductor character, crystallinity, and degree of functionalization. Herein, structural quality of pristine V-CNTs and H-CNTs was the only consideration through a graphite/defect (G/D) frequency range.

Fluorescence microscopy
Exposed amine groups on CNTs were evaluated using FITC conjugation. 100 μg/mL of FITC was dissolved in acetone and C2H2 and NH3 plasma-treated CNTs was immersed into FITC solution for 1 hr. The CNTs was washed 5 times with DI water and observed fluorescence signal by using fluorescence microscope.

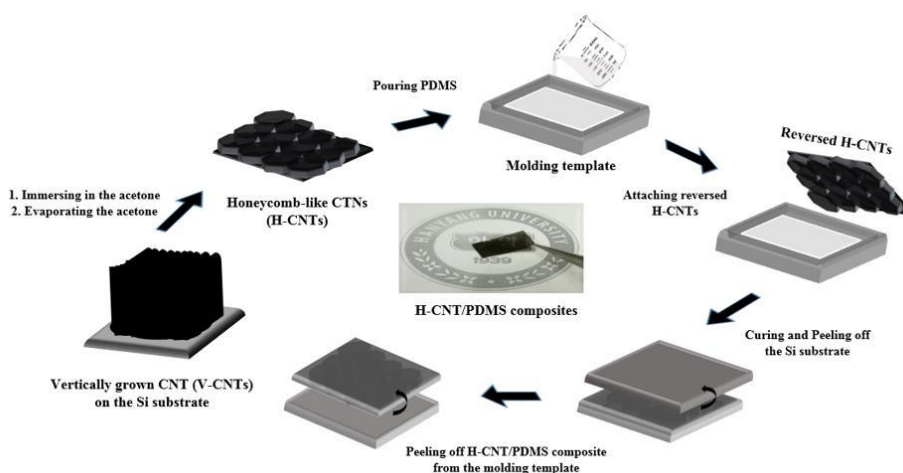**Plasma treatment and XPS analysis**

Same with the process mentioned in part 1.4.

Quantification of Cyfra 21-1
Same with the process described in 2.2
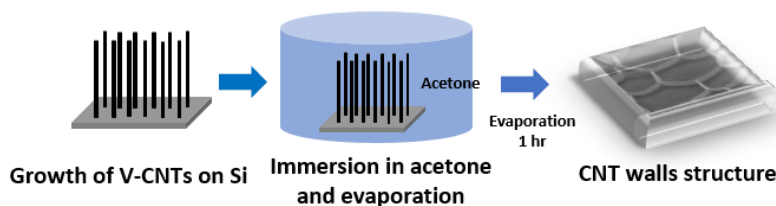
Scheme 5. Scheme of solvent-assisted CNT wall structure formation

Scheme 6. Schematic illustration of flexible sensor fabrication.

Results and Discussion

Characterization of V-CNT and H-CNT Structures

The surface morphology of H-CNTs resulted from capillary forming was analyzed by using SEM. Prior to the formation of H-CNTs, V-CNTs were synthesized by using LP- TCVD and was directly immersed in the acetone to form H-CNT structure. The acetone wetted the CNTs independently within each CNT microstructure due to capillary action. Furthermore, acetone was evaporated to initiate capillary densification of CNTs. In this study, the immersion method was used due to its simplicity compared to the other methods. The acetone was chosen as the most suitable solvent to form a shrunken CNT structure. The H-CNTs formed by the capillary driven force self-assembly displayed honeycomb-like patterns which have a width around 5-30 μm as shown in Figure 22. As depicted in Figure 23a and 23c, H-CNT structures have a lower height (5 μm) compared to the as-grown V-CNT (24 μm) due to shrinking CNT during the capillary self-assembly process. The formed H-CNT structure also has bundle shape with an average diameter of 23 nm, and it is two time larger than the as-grown V-CNT as shown in **Figure** 23b and 23d.

The bundle formation on H-CNT structure could be caused by van der Walls forces between CNT. However, the pattern of H-CNT was uncontrollable and tricky due to a complicated forces mechanism, therefore, the resulting structures showed irregular patterns formation.

Figure 22. Morphology images of CNT wall structures
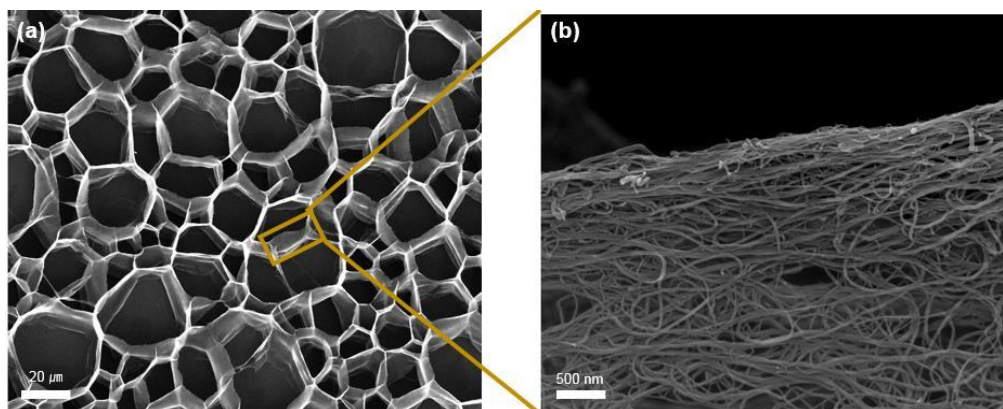
The densification step during H-CNT formation process may damage the CNT of the as-grown V-CNT. The damage could be known by the present of swift D/G band ratio between the as-grown V-CNT and formed H-CNT. Thus, Raman analysis with a micro- sized laser-beam was conducted to investigate the quality of formed H-CNT structure. The as-grown V-CNTs displayed the D/G band ratio of 0.71. The RBM peak was not found on as-grown V-CNT, thus, it means that the as- grown V-CNTs was MW-CNTs. As shown in Figure 24, the Formed H-CNTs structure displayed a similar D/G band ratio with as-grown V-CNTs (0.71). Therefore, it could be assumed that the CNT was not damaged during the densification step on the H-CNT formation process. Figure 25shows that the surface of CNT wall structures on Si substrate was functionalized with amine groups under the various conditions of RF-plasma treatment and the density of amine groups is well controlled and confirmed. Figure 26 shows that the detection sensitivity of Cyfra21-1 antigen using CNT wall platform is similar with that of 3DCNW platform. With the CNT wall structures, the surface modification with various functional groups could be well controlled.

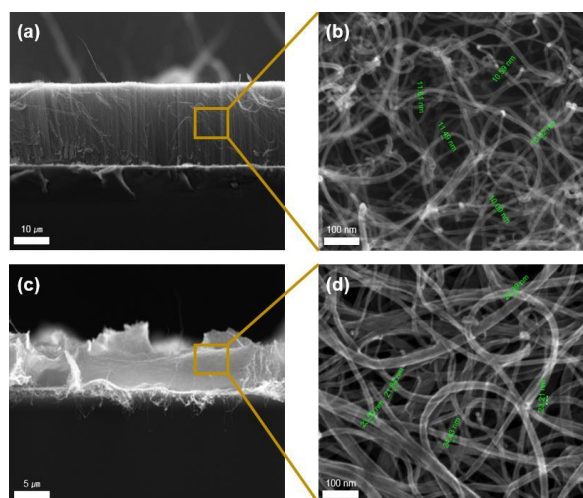Figure 23.SEM images of (a) side view image of V-CNTs and (b) corresponding high-resolution image of V-

CNTs. (c) side view image of H-CNTs and (d) corresponding high-resolution image of H-CNTs.
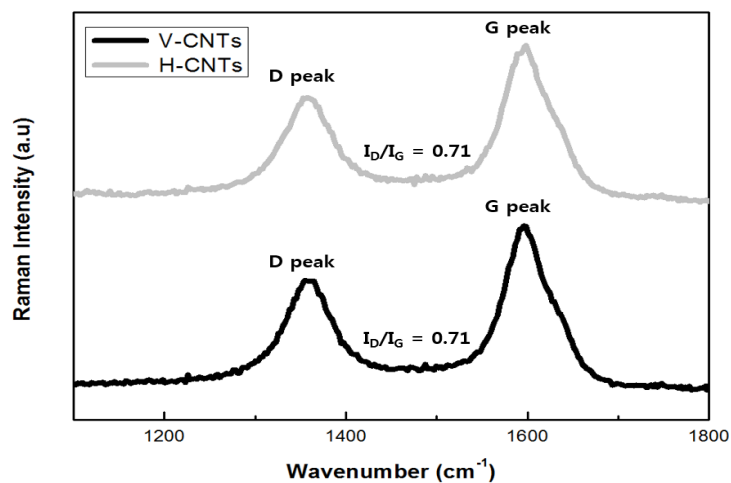

Figure 24. Raman spectra of V-CNTs and H-CNTs
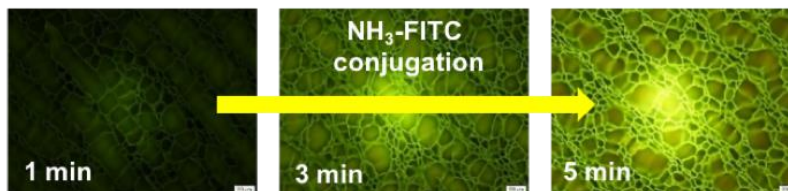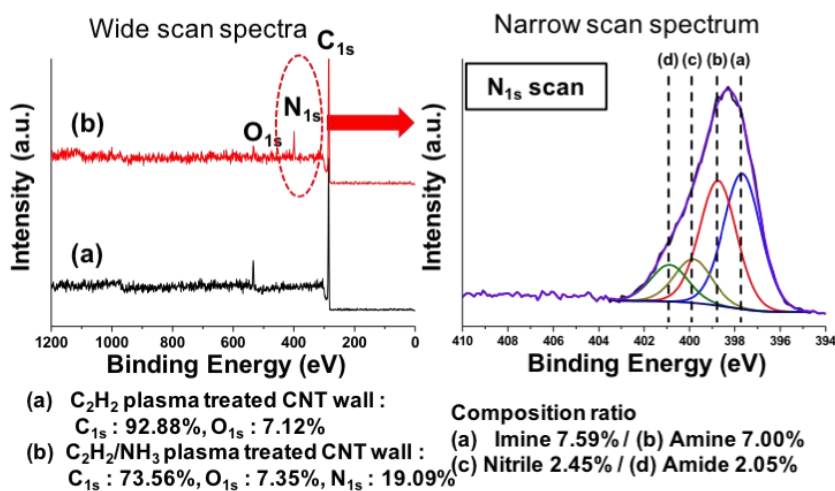
Figure 25. XPS analysis of CNT wall structures after plasma treatment and Fluorescence intensity of FITC probe conjugated with   amine groups was monitored at various plasma conditions
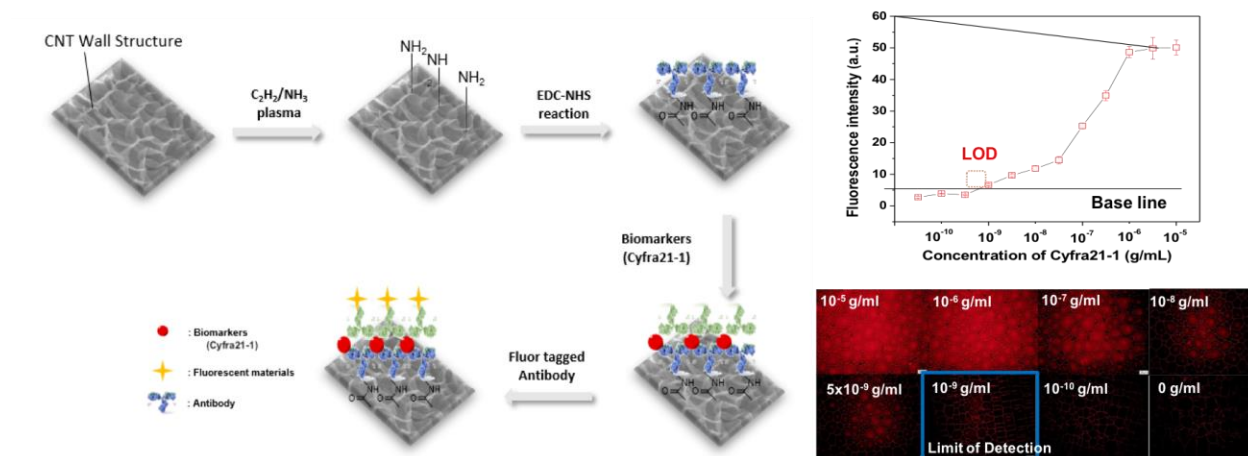
Figure 26. Fluorescence-based immunoassay by using CNT wall structures for quantitative analysis of Cyfra 21-1.

Conclusion

For exploring CNT-based biosensor or CNT-embedded strain sensor in flexible devices, a new platform in which a noble CNT wall structure is gently embedded onto the upper part of PDMS film. The detection of Cyfra 21-1 biomarker on CNT wall structures is quite excellent as like as that of 3DCN structures. The fluorescence microscope images are all excellent. The impact of a CNT wall structures embedded PDMS film is quite high and promising as a highly sensitive and cost-effective flexible sensor.

3. Third Year Progress

In the third year, we continue the development of 3DNCW template for sensing biomolecules. We also investigated a simple and efficient label-free bacterial detection system using the polydiacetylene (PDA) liposomes immobilized on a novel 3D PDMS micropillar substrate.

3.1. 3DCNW structures for early detection of cancer biomarkers

Introduction

Cancer antigen 125 (CA125) is a biomarker frequently used for ovarian cancer detection. Elevated levels of CA125 in human body fluids such as blood and saliva in specific types of cancers and diseases as well as in ovarian cancer make this protein a useful biomarker for essential diagnosis and therapeutic monitoring. In addition, combinations of CA125 with several multiple biomarkers have shown increased diagnostic specificity for the onset or recurrence of cancer in clinical practice. Nonetheless, commercial enzyme-linked immunosorbent assay (ELISA) kits or other dual antibody-based assays from different manufactures often have limited detection sensitivity and selectivity, which impedes the reliable use of CA125 in early cancer diagnosis. Nucleic-acid aptamers are single-stranded DNA (ssDNA) or RNA molecule selected *in vitro* that are potential alternatives to antibodies. Unlike antibodies, they can bind a broad range of target molecules, are easy to modify, have high chemical stability, and can be produced on a large scale, making them attractive for molecular diagnostic and therapeutic applications. Given appropriate aptamer-aptamer or aptamer-antibody pair in conjunction with sensing platforms, reliable and sensitive detection of CA125 target proteins can be achieved. Herein, we report the selection of an antiCA125 ssDNA aptamer and its application to sensitive detection of CA125 when used together with a CA125-specific antibody immobilized on 3DCNWs. With exceptional stability and easy modifications over antibodies, the selected ssDNA aptamer (rCAA-8) showed high binding affinity (166 nM) for recombinant CA125, which enabled CA125-specific imaging in ovarian cancer cells (OVCAR-3). Furthermore, when compared to other fluorescent assays based on graphene oxide or flat surface and traditional enzyme-linked immunosorbent assay, a chip-based assay using a 3DCNW surface and anti-CA125 antibody-aptamer pair resulted in higher sensitivity and broader dynamic range as a function of CA125 concentration, due to high target specificity and high surface loading density. Our on-chip aptamer-based assay will facilitate sensitive and specific monitoring of CA125 in the biological and clinical fields.

Materials and methods

Materials
Recombinant human CA125, mouse anti-CA125 monoclonal antibody, and FITC conjugated rabbit anti-MUC16 polyclonal antibody were purchased from Fitzgerald. Recombinant human CA125/MUC16 protein was purchased from R&D systems. OVCAR-3 and SK-OV-3 cells were purchased from the Korean cell bank. SELEX library and primers were

synthesized by Macrogen (Korea). pGEM-T Easy vector system was purchased from Promega (USA). Ni-nitrilotriacetic acid (Ni- NTA) spin columns, NeutrAvidin-horseradish peroxidase (HRP), NeutrAvidin-agarose beads, tetramethylbenzidine (TMB) substrate solution, and Dulbecco's phosphate-buffered saline (DPBS) were purchased from Thermo Scientific (USA). Bovine serum albumin (BSA), N-(3-dimethylaminopropyl)-N'-ethylcarbodiimide hydrochloride (EDC), N-hydroxysuccinimide (NHS), graphene oxide (dispersed in H_2O), and Tween-20 were purchased from Sigma Aldrich. $Fe(NO_3)_3 \cdot 9H_2O$ and AEAPDMS were purchased from Junsei (Tokyo, Japan). Mo solution was purchased from Aldrich Chemicals Co.. Aptamers labeled with biotin at the 5'end or 6-carboxy-fluorescein (6-FAM) at the 3' end were synthesized by IDT (USA). All other reagents were purchased from commercial sources and were of the highest grade available.

Primers and ssDNA library amplification
A forward primer (5'-ATGCGGATCCCGCGC-3') primer labeled with biotin (5'-B-C6-CGCAAGCTTCGCGCG-3') were used to amplify the random ssDNA library (GCGCGGATCCCGCGC-N30-CGCGCGAAGCTTGCG) by polymerase chain reaction (PCR). The biotinylated-PCR product was then incubated with NeutrAvidinagarose beads in phosphate-buffered saline (PBS) for 1h at RT with shaking, which was followed by three washes with PBS. ssDNA was eluted with 0.15 M NaOH and purified using ethanol precipitation after neutralization with 0.3M potassium acetate buffer (pH 3.0).

SELEX procedure
In vitro SELEX was carried out with His6-tagged rCA125 and a random ssDNA library. Prior to SELEX, 500 ng of the ssDNA library was pre-incubated with 100/L of Ni–NTA sepharose beads in binding buffer (30 mM Tris–HCl (pH 7.5) containing 50 mM NaCl, 1.5 mM MgCl2 and 0.1% BSA) for 30 min at RT with shaking. After removing the ssDNA non-specifically bound to beads by centrifugation, the supernatant was incubated with 2μg of rCA125 for 60 min at 37 ⃞ C in the same binding buffer. The reaction mixture was then loaded onto a Ni–NTA spin column and incubated for another 30min at RT. The column was washed five times with washing buffer to remove unbound ssDNA. The bead-bound ssDNA-rCA125 complex was eluted with imidazole elution buffer. The ssDNA bound to the CA125 was then recovered using phenol–chloroform extraction and ethanol precipitation. The recovered ssDNA library was amplified by PCR and used for the next round of selection. After three consecutive rounds of selection in the same manner, stringent conditions including reduced ssDNA concentration, reduced binding time, and increased NaCl concentration were employed. To further reduce non-specific binding of the ssDNA library, negative selection was performed at the 4th and 8th rounds using BSA and NTA beads without rCA125. Enrichment of aptamer pools in subsequent rounds was monitored using band intensities in agarose gels. After the 10th round, the SELEX product was amplified by PCR and cloned into a pGEM-T Easy vector. Insert-transformed plasmid DNA was isolated from individual clones and DNA sequences were analyzed. The secondary structures of potential aptamers were predicted using the mfold web server with default parameters of 21°C, 100mM Na^+, and 1.5 mM Mg^{2+}.

Determination of binding affinity

Initially, the ability of aptamers to bind to CA125 was analyzed using a 96-well plate-based assay. Briefly, 0.5 g of rCA125 diluted in PBS was added to each well in the 96-well plate for 1h at RT with shaking. Wells were washed three times with PBS containing 0.05% Tween-20 (PBST) and various concentrations of biotin-labeled aptamers were added, followed by another 1 h incubation at RT with shaking. Wells were then washed three times with PBST and incubated with NeutrAvidin-HRP (diluted 1:8000 in PBST) for another 30 min. After thoroughly washing the wells with PBST, TMB solution was added to quantify the binding of rCA125 to the aptamer. The colorimetric reaction was stopped with H_2SO_4 and the corresponding absorbance at 450 nm was measured using a multimode plate reader. To determine the binding affinities of the selected aptamers, further analysis was performed using biolayer interferometry. Prior to binding measurements, a streptavidin-coated optical probewas equilibrated for 10 min in loading buffer. After obtaining the initial base line for 30s, a biotinylated aptamer was loaded onto the streptavidin-coated sensor for 120 s. The biosensor was washed for 30 s by flowing through the loading buffer and equilibrated with binding buffer for another 60 s. The rCA125 protein was then associated for 120 s, followed by dissociation for another 120 s in binding buffer. Dissociation constants (KD) were generated by fitting the data to a 1:1 binding model using a BLItz Pro software.

Cell imaging using aptamers
Both OVCAR-3 (CA125-positive) and SK-OV-3 (CA125-negative) cells were cultured in T25 tissue culture flasks in RPMI-1640 medium containing 10% FBS at 37 °C. When cells reached 80% confluence, they were harvested by trypsinization and newly seeded onto an 8-well chambered slide glass for 24 h. Cells were then briefly rinsed three times with PBS and fixed using either 100% methanol for 5 min or 4% paraformaldehyde in PBS for 10 min at RT. After thoroughly washing three times with ice-cold PBS, FAM-labeled aptamers were added to the slides at different concentrations in a final volume of 200 L in DPBS, followed by a 1 h incubation at RT. Cells were then washed three times with DPBS, and one drop of VECTASHIELD mounting medium with DAPI was added to each well to stain the cell nuclei. Fluorescence images were acquired using a confocal microscope. Excitation/emission wavelengths of DAPI and FAM were 408/447 nm and 488/525 nm, respectively.

Graphene oxide (GO)-based assay
The stock solution of GO was diluted at appropriate concentrations using binding buffer. For the florescent detection, rCAA-8-FAMand GO ($50 \mu gmL^{-1}$) were incubated at RT with shaking for 15min. The optimal GO concentration ($50 \mu gmL^{-1}$) and incubation time (15 min) were determined after being tested to quench above 90% fluorescence intensity of rCAA-9-FAM aptamer. To assay CA125, different concentrations of rCA125 were added to the mixture of GO/rCAA-8-FAM and incubated for another 30min. The fluorescence intensities were measured at a 96-well microplate using a multiplane reader at an excitation filter of 490 and emission wavelength of 518 nm.

Preparation of a CA125 biosensor platform using 3DCNWs
3DCNW was prepared as described previously. The height and diameter of the as-prepared Si pillars were 15 and $2 \mu m$, respectively. The distance between Si pillars was $2 \mu m$ or tunable. 3DCNWs were synthesized by thermal chemical vapor deposition system using NH_3 gas for 10min followed by C_2H_2 gas at 850 °C for 20 min. The morphology of the 3DCNW template

was assessed by FE-SEM. Si pillar templates with CNTs were coated with a 15-nm-thick aluminum oxide layer by atomic layer deposition to preserve the structural properties of the template during immunoassay. The saline compound AEAPDMS was used as a starting molecule for the formation of an SAM on the surface of the ALD-modified 3DCNWs or ALD, and mouse anti-CA125 was subsequently conjugated to the template by EDC/NHS reaction. As a control surface, AEAPDMS-modified silicon surface (2D-SAM) was used. Five micro-liters of 1mM EDC and 4mM NHS were added to 990uL PBS (pH 7.4) containing 10μg of mouse anti-CA125 and pre-reacted at 50rpm for 15min. The amine-functionalized substrate was transferred to the wells of a 96-well plate and incubated with crosslinking solution for 3h at 25℃. After the reaction, the substrates were washed with washing solution to remove excess reagent and non-binding antibodies.

Evaluation of CA125 detection using the aptamer/3DCNW platform
To quantify CA125 on the antibody-immobilized 3DCNWs (or 2D-SAMs), a fluorescence-based sandwich assay was performed using either rCAA-8-FAM or scramble-FAM aptamer as a detection probe. The substrates with mouse anti-CA125 antibody immobilized were exposed to various concentrations of CA125 in PBS ranging from 10^{-12} to 10^{-6} g mL^{-1} for 1 h, and then the surface was washed five times with washing solution. Each sample was incubated in 50 uL of 10 μM rCAA-8- FAM or scramble-FAM aptamer for 1 h, and then unbound aptamer was removed by washing. Fluorescence images were obtained using an Olympus BX51W1 fluorescence microscope with a 50× objective lens and analyzed using ImageJ software.

Results and Discussion

SELEX
Affinity-based SELEX process was performed using a library of ssDNA molecules composed of two primer regions and a 30-nucleotide random region to select CA125-specific aptamers. The hexahistidine (His6) tag of recombinant CA125 (rCA125) allowed the use of Ni-NTA sepharose beads to bind this protein, which was followed by iterative cycles of capturing bound ssDNA, removing unbound ssDNA, eluting protein-bound ssDNA, and amplifying the desired ssDNA obtained by SELEX using stringent conditions such as low ssDNA concentration, short binding time, and high salt concentrations. To reduce the non-specific binding of ssDNA, negative selection was performed at the 4th and 8th rounds using bovine serum albumin (BSA) and NTA beads. The ssDNA pools reached steady binding after 10 rounds of selection and amplification, as evidenced by the lack of a significant difference in band intensity on agarose gels between the last two successive selected pools (data not shown). The nucleotide sequences of 50 clones were determined and aligned using the web-based tool ClustalW. Along with this alignment of ssDNA sequences, we chose three distinct ssDNAs (termed rCAA-8, rCAA-11, and rCAA-13) based on their frequency and homology to the primary sequences (Table 1). Prediction of the secondary structure of three selected ssDNAs using mfold revealed that all truncated aptamer candidates

contained one or more loops, which is independent of primer binding sequences, with some similarity in the sequences of the ssDNAs at their 5' ends (Figure 27).
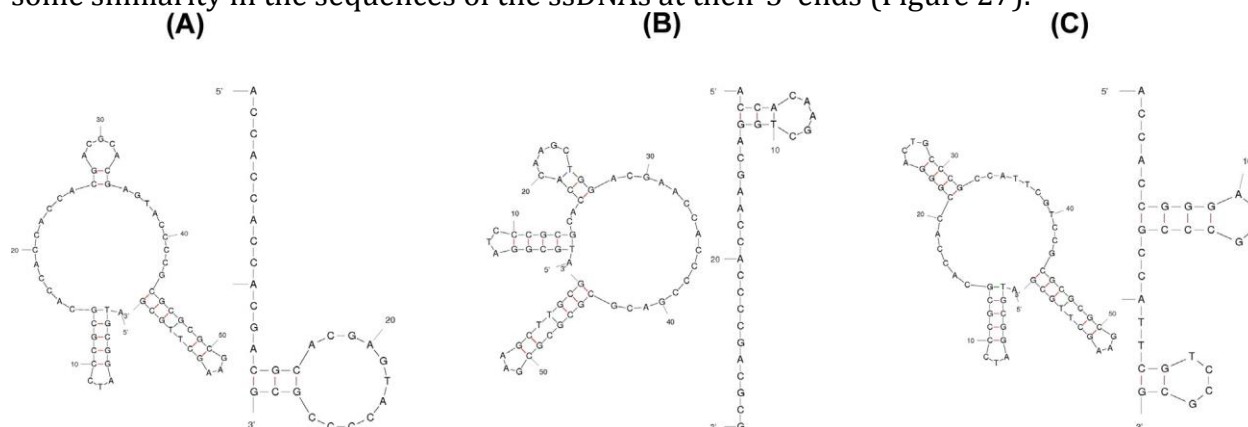

Figure 27. Predicted secondary structures of (A) rCAA-8, (B) rCAA-11, and (C) rCAA-13. The full-length aptamers including primer binding sites at the 5' and 3'-end (left) and truncated forms without primer binding sites (right) were displayed.

Although the secondary structures of full-length aptamers including primer binding sites appear greater than those of truncated variants, the sequence at the 5' and 3' end for primer binding site was considered as an insignificant region to the binding event (data not shown). The □G values of clones rCAA-8, rCAA-11, and rCAA-13 were −1.77, −2.07, and −4.05 kcal mol−1, respectively. CA125 is a glycan-rich protein with numerous splicing variants that range from 1148 to 22,152 amino acids in length and from 200 to 5000 kDa in size. Full-length CA125 (22,152 amino acids) consists of an exclusively O-glycosylated N-terminal domain (12,000 amino acids), a tandem repeat domain (up to 60 repeats of 156 amino acids each harboring O- and N-glycosylation sites in which each unit includes a sea-urchin, enterokinase and agrin (SEA) domain), a transmembrane domain, and a cytoplasmic tail of 32 amino acids. The rCA125 antigen used in this study represents amino acids 21,712–21,973 of the full-length sequence and includes the final repeated SEA domain, which is well conserved evolutionarily according to the product manufacturer. Although the tertiary structures of these DNA aptamers remained undetermined in the present study, we assume that the single loop regions in the aptamer candidates play a significant role in allowing these aptamers to associate with repetitive domains of rCA125 which have conformation-sensitive, structures, thus providing a sufficient binding pocket for ssDNA.

Determination of binding affinity
To investigate the binding of aptamers to CA125, direct ELISA was performed in a 96-well plate, in which 0.5μg rCA125 was initially adsorbed to the surface of each well, followed by block- ing with 2% BSA. Various concentrations (0.15–10μM) of the 5'-end biotinylated aptamer were then added to each well. When NeutrAvidin-conjugated horseradish peroxidase (NA-HRP) and its substrate were subsequently used for colorimetric detection, sig- nal increased in a dose-dependent manner according to aptamer concentration (Figure 28A). Among the three aptamer candidates eval- uated (rCAA-8, rCAA-11, and rCAA-13), rCAA-8 showed the highest binding ability based on colorimetric signal intensity at 450 nm; the intensity of rCAA-8 was almost two-fold higher than that of rCAA-11, and slightly higher than that of rCAA-13 over the

tested concentrations (Figure 28B). Control experiments without rCA125 showed negligible signal intensity when compared with CA125-coated wells. Saturation was obtained at rCAA-8 concentrations higher than 5 µM.
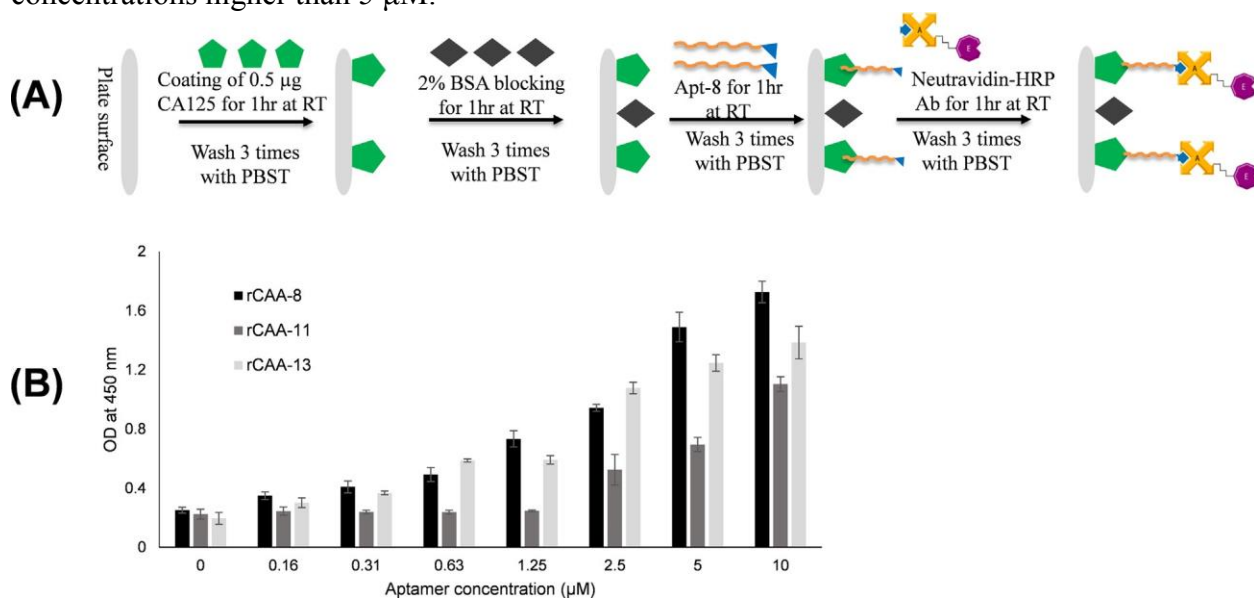

Figure 28. Dose-dependent binding of candidate aptamers to rCA125 in a 96-well microplate. (A) Scheme of detection process and (B) the corresponding graph obtained by analysis of HRP-induced colorimetric data. Standard deviations in (B) were obtained from two independent experiments.

To determine the binding affinity of the selected aptamers, association and dissociation rate constants of the aptamer for rCA125 were analyzed using biolayer interferometry (BLI) in a real-time manner. This technique measures the shift in the interference pattern of the reflected light between two layers (biomolecule-binding layer and internal reference layer) on a disposable fiber optic-based surface. This shift is directly correlated to the distance or optical thickness between two reflective layers when a number of molecules bind to the surface, leading to a change in BLI sensing units in relation to a nanometre-scale shift in wavelength. rCA125 protein was flowed over the surface-immobilized ssDNA aptamer. When biotinylated aptamers were loaded onto streptavidin-coated optical biosensors and further subjected to rCA125 binding, the three selected aptamers showed strong associations with rCA125 (Figure 29A) compared with BSA (Figure 29B). The initial binding affinities of ssDNA aptamers were slightly different between Figure 29A and B, presumably due to variations in streptavidin-coated sensors. Among the aptamers, rCAA-8 had the highest binding affinity for rCA125 with a KD value of 166 nM (based on association/dissociation rate constants) (Table 1). These data correlated well with those of a plate-based assay, as shown in Figure 28, indicating that the selected ssDNA aptamer (rCAA-8) is suitable for the detection of CA125 with high affinity. A series of DNA and RNA aptamers against CA125 generated by SELEX was also very recently reported, which focused upon its distinct SELEX process. This binding affinity for rCAA-8 for CA125 in this study was comparable to that reported for the other DNA aptamer and lower than that of the RNA aptamers (KD ~ 4 nM). There was no sequence similarity between our DNA aptamers and those reported previously, which we attribute to differences in the CA125 antigen used in SELEX (recombinant CA125 protein for the current work and native CA125 protein from human ascites fluid in the previous study).
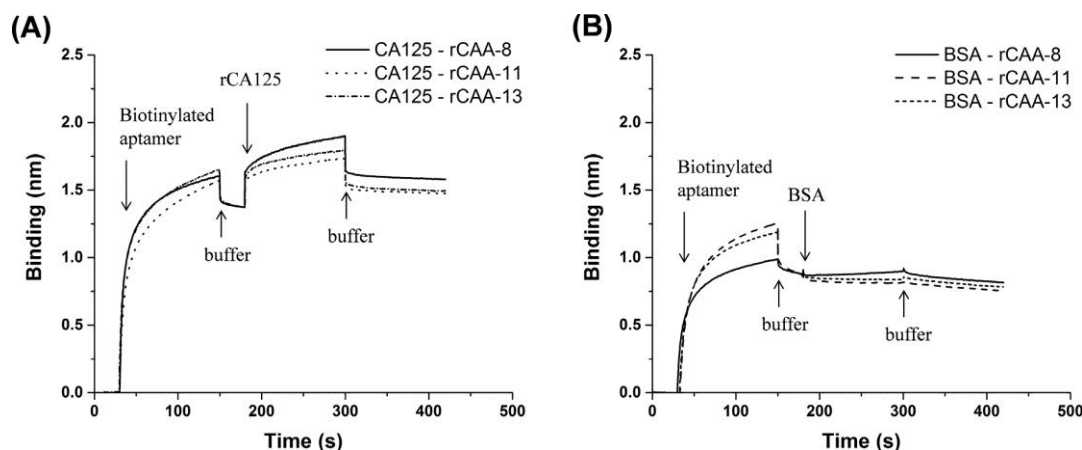
Figure 29. Dose-dependent binding of candidate aptamers to rCA125 in a 96-well microplate. (A) Scheme of detection process and (B) the corresponding graph obtained by analysis of HRP-induced colorimetric data. Standard deviations in (B) were obtained from two independent experiments.

Cell imaging with aptamers

We further investigated whether rCAA-8 could bind to CA125 expressed on the membrane of ovarian cancer cells using fluo- rescence imaging. To do this, CAA-8 aptamers were labeled with 6-carboxy-fluorescein (6-FAM) at their 3′ ends (5′-ACC ACC ACC ACG ACG CAC GAG TAC CCC GCG-6-FAM-3′) and incubated with both CA125-positive ovarian cancer cells (OVCAR-3) and CA125- negative ovarian cancer cells (SK-OV-3) for 1 h after fixation. As a negative control, scramble aptamer labeled with 6-FAM (5′-GTC CAA CGC CAA CGC AGC CGA CCG ACC ACC-6-FAM-3′) was used. As shown in Figure 30, FAM-labeled rCAA-8 aptamer gave rise to a strong fluorescence signal in OVCAR-3 cells based on confocal imaging (Figure 30A), whereas neither the scramble aptamer in OVCAR-3 (Figure 30B) nor the rCAA-8 aptamer in SK-OV-3 (Figure 30C) resulted in significant fluorescence on the cell surface. When OVCAR-3 cells were treated with various concentrations (200 nM - 2 μM) of the CA125-specific aptamer, a significant increase in mean fluorescence intensity was observed on the cell surface as the aptamer concentration increased. In contrast, negligible fluorescence was observed over the same concentration range of irrelevant aptamer (scrambled aptamer). These results suggest that the rCAA-8 aptamer was associated specifically with CA125 expressed by ovarian cancer cells. Since there were no fluorescent images observed in cell nuclei or cytosol, our aptamer is revealed to target CA-125 located in cellular membrane.

Assaying CA125 based on aptamer/3DCNW platform

To use the aptamers generated in a bioassay, we constructed sandwich-type assays to detect CA125 based on antibody-aptamer pairs using a 3D network of carbon nanotubes (3DCNWs). Because the surfaces of 3DCNWs can be loaded with capture molecules at a high surface density, this system should be sensitive to low abundance targets, leading to improved detection limits when compared to conventional immunoassays on a surface or ELISA. When aptamer pairs of the three candidates were tested in sandwich- type assays on a plate, rCAA-8 aptamer and the other aptamers showed no differences in signal in the presence of CA125, indicating that three aptamer candidates recognize similar binding sites

of CA125. It is complicated to choose antibody pairs for a target because of factors such as high cost, antibody instability, and cross-reactivity. In addition, to avoid overlap in the CA125 epitope, we used CA125 (110 kD) with more SEA domains than are used in SELEX (33 kD), because the capture antibody (anti-CA125 mAb) in this study belongs to group A, like OC125, which is known to bind to different regions of CA125 than aptamers. In addition, in case that the aptamer is immobilized on the 3DCNW surface as a capture molecule, the detection sensitivity for CA125 may decrease, due to its low affinity binding than that of capture antibody. Therefore, we reasoned that an antibody-aptamer pair (an antibody and an aptamer can act as a capture molecule and a detection molecule, respectively) could be used to detect CA125 in a sandwich man- ner with high sensitivity.
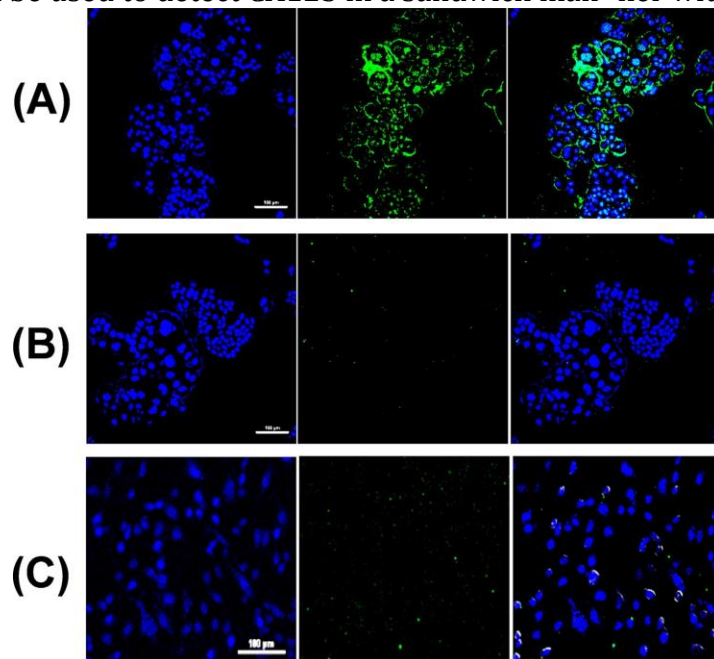

Figure 30. Cell targeted using FAM-labeled anti-CA125 aptamers. (A) rCAA-8-FAM aptamer (5′-ACC ACC ACC ACG ACG CAC GAG TAC CCC GCG-6-FAM-3′) detection of CA125- positive OVCAR-3 cells, (B) scramble-FAM aptamer (5′-GTC CAA CGC CAA CGC AGC CGA CCG ACC ACC-6-FAM-3′) detection of OVCAR-3 cells, and (C) rCAA-8-FAM aptamer detection of CA125-negative SK-OV-3 cells. Left (DAPI nuclei staining), middle (FAM imaging), and right (superimposed) panel images were obtained at a final aptamer concentration of 1 μM. The white scale bar represents 100 μm.

As illustrated in Figure 31A, a monoclonal anti-CA125 antibody (anti-CA125 mAb) was immobilized to 3DCNW surfaces or 2D-SAM surface (control surface) as a capture probe for rCA125, while the selected aptamer (rCAA-8, labeled with 3′-FAM) was used as a detection probe for rCA125. The CNT net- work was constructed between Si pillars (15um in height and 2 μm in diameter), which was followed by aluminum oxide coating by atomic layer deposition and treatment with a self-assembled monolayer with an amine-ended group to immobilize the anti-CA125 mAb. When the mean fluorescence intensity of rCAA-8-FAM aptamer was measured after completing the CA125-binding reaction in a scanned area of 210 × 280 μm2 on the 3DCNW platform, a notable linear increase in fluorescence was observed as a function of CA125 concentration (from 1 pg mL−1 to 1 μg mL−1) (Figure 31B (i)). In contrast, the scramble aptamer labeled with FAM on the 3DCNWs (Figure 31B (ii)) and the FAM-labeled rCAA-8

aptamer on the 2D-SAMs (Figure 31B (iii)) showed no increase in fluorescence over the tested CA125 range. In Figure 31C, the linear plot ($R^2 = 0.996$) shows the sensitive detection limit (as low as 10 pg mL^{-1} based on 3×standard deviation) and wide dynamic range (5-order range from 10 pg to 1 μg mL^{-1}) of this platform. These values are better than those reported by fluorescence-based immunoassay and the limit of detection (LOD) is approximately 106–fold higher than that (20 μg mL^{-1}) by graphene oxide (GO)-based fluorescent assay when the GO was incubated with rCAA-8-FAM as a function of CA125 concentration. Most significantly, the sensitivity was approximately 103–fold higher than that (7 ng mL^{-1} in Figure 31D) by classic ELISA using two antibodies. Considering that fluorescent data on the 2D-SAM surface showed a similar sensitivity with that of ELISA, the dramatic increase in fluorescence intensity on the 3DCNW surface is attributed to distinct surface structure of CNT network. It is important to note that the 3DCNWs enabled signal enhancement at a relatively low concentration (below μg mL^{-1}) of target, as reported previously. These results indicate that the antibody-aptamer pair bound to CA125 without cross-reactivity, and that this sandwich assay using 3DCNWs allowed detection of CA125 with high sensitivity. Although the detection sensitivity for CA125 using the antibody-aptamer pair was comparable to that of an antibody–antibody pair on the same 3DCNWs (data not shown), this aptamer has a great potential as a detection probe with high stability and easy modification.

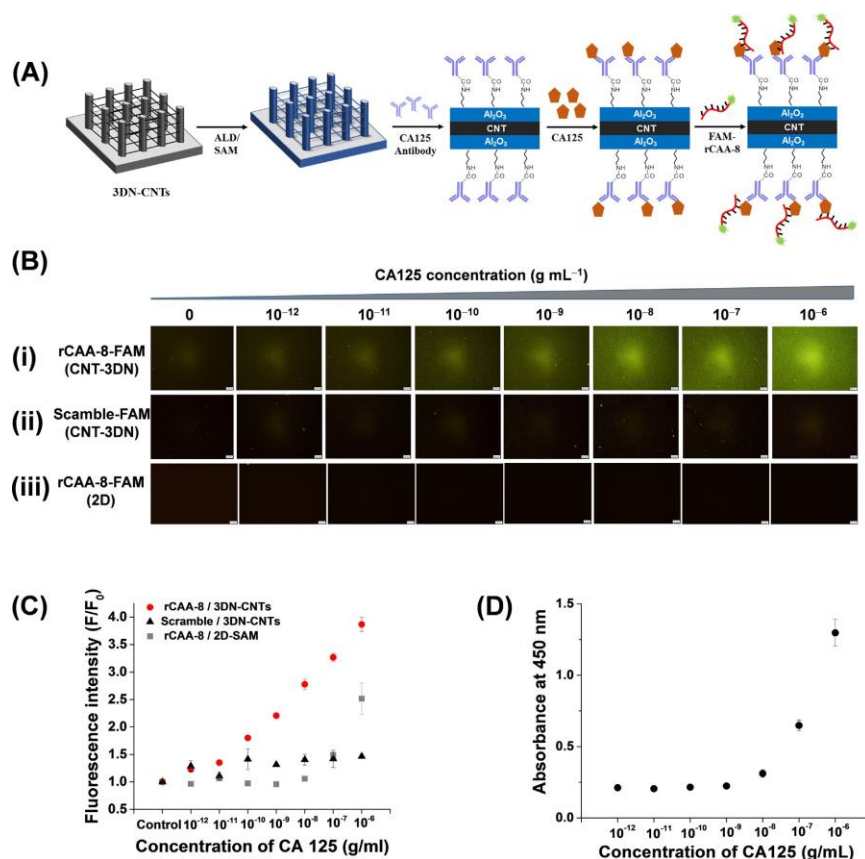Figure 31. (A) Schematic illustration of fluorescence-based detection of CA125 using aptamer-antibody pair on 3DCNWs. (B) Microscopic fluorescence images from i) rCAA-8-FAM/3DCNWs, ii) scramble aptamer-FAM/3DCNWs, and iii) rCAA-8-FAM/2D-SAMs. The white scale bar represents 20 μm. (C) Plotted curves corresponding to (B) from rCAA-8 aptamer/3DCNWs (circle), scramble aptamer/3DCNWs (triangle), and

rCAA-8 aptamer/2D-SAMs (square) as a function of CA125 concentration. (D) Standard curve from a traditional ELISA using two antibodies as a function of CA125 concentration. The error bar indicates the standard deviation, which was calculated based on three independent experiments.

Conclusions

We described the selection of an anti-CA125 aptamer and its application to a biochip involving a three-dimensional network of carbon nanotubes (3DCNWs) to detect CA125. The aptamer, rCAA- 8, showed high binding affinity for the repetitive domain of CA125, allowing discrimination of CA125-expressing cells (OVCAR-3) from CA125-negative cells (SK-OV-3) by fluorescence imaging. Compared to traditional ELISAs for CA125, the aptamer-based CA125 assay on the 3DCNWs showed higher sensitivity and a broader dynamic range as a function of CA125 concentration, due to high target specificity and high surface loading density. Selected aptamers can highly facilitate the detection of CA125 in the clinical setting.

3.2. Immobilized polydiacetylene lipid vesicles on PDMS micropillars as a surfactin-based label-free bacterial sensor platform

Introduction

Many bacteria are harmful pathogens in several plants and animals including human beings. However, certain bacterial strains are used as materials for genetic engineering and an industrial workhorse for the economic production of numerous enzymes, proteins, and antibiotics. B. subtilis as a model of Gram-positive bacteria have been intensively characterized in a variety of ways for the microbiological research as well as biotechnology. It is worth developing sensing materials to detect B. subtilis by using the surfactin as an indirect mediator. Rapid detection method technologies have been developed such as PCR technology, ELISA and immunomagnetic separation method. Critically, these techniques are generally time-consuming and costly due to the requirements of particular types of equipment and reagents. New types of detection methods have been made possible through biosensors. Biosensors is a rapid and cost-effective method that combine biomaterial compounds with a physicochemical transducer with the ability to obtain a measurement with minimal perturbation of the sample. The recognition of the biomaterials in biosensor can be achieved either by using a label or label-free systems. Labels have been essential in bioanalytical research; however, this technique has several drawbacks such as only providing an endpoint reading, noncontinuous monitoring, and multiple washing stages, thereby reducing throughput effectivity and increasing the cost. Due to these considerations, the development of label-free biosensors that can reduce assay cost and complexity while providing quantitative information with high throughput effectivity is an important research goal.

Polydiacetylene (PDA)-based sensor as label-free bacteria detection has been intensively investigated due to its unique stimulus-induced significant color-changing properties from brilliant blue to red. However, the majority of the PDA-based sensors that have been reported were prepared in the form of a liposome in aqueous solution or thin film as two dimensional

(2D) structures. The high selectivity of amine functionalized PDA solutions toward surfactin has been reported in a number of works.

Our previous works reported the immobilization of PDA liposomes onto hierarchical 3D networked nanostructures to overcome the intrinsic limitations of the 2D system and affords a significant increase in the sensitivity of PDA. In this work, we investigated a PDA vesicle-based sensor on PDMS micropillars (3D-PDA-PDMS) for detecting B. subtilis. In order to develop immobilized polydiacetylene vesicles on polydimethylsiloxane micropillars (3D-PDA-PDMS), amine functionalized diacetylene monomers PCDA-EDEA and PCDA- EDA were prepared. The mixture of PCDA-EDEA and PCDA- EDA, which has different lengths of amine ligands and has gaps along the length of its hydrophilic exterior, can ensure a better adherence and reaction. The assembled vesicles of PCDA-EDEA and PCDA-EDA were formed with the molar ratio 1:1, which is the optimal mixture ratio. The chromatic change in PDA caused by the surfactin was used as an indirect sensing method to readily detect the presence of bacteria and a high throughput screening tool for certain bacterial strains that produce surfactin. PDMS was used to fabricate a micropillar template by controlling the diameter, height, and gap of the pillars.

Materials and Methods

The Fabrication of PDMS Micropillars
A three-dimensional pillar silicon wafer was used as the master mold. The uncured PDMS mixture was poured on the master mold and cured at 80◦ C for an hour. After cooling down the process, the hole patterned-PDMS was detached from the master mold. Before undergoing second step molding, the hole patterned-PDMS mold was exposed to UV-ozone cleaner for 10 min to decrease the hydrophobicity for further modification. The UV-ozone treated hole patterned-PDMS molds were treated with OTS in an ethanol solution for 30 min under nitrogen atmosphere. The substrate was washed several times with ethanol. The uncured PDMS mixture was poured on the OTS treated hole patterned-PDMS mold and cured at 80◦ C for an hour. After the cooling down process, the micropillar PDMS was peeled off from the hole patterned-PDMS mold.

Preparation of diacetylene vesicles
The amine-terminated diacetylene monomers PCDA-EDEA and PCDA-EDA were synthesized by employing standard procedures. A mixture of EDEA and EDA terminated diacetylene monomers were dissolved in chloroform in a test tube. The solvent was evaporated by a stream of N2 gas, and deionized water was added to the test tube to give the desired concentration of lipid (1mM). The resultant suspension was sonicated for 15 min at 80◦ C followed by filtering for removing dispersed lipid aggregates by using a 0.8 μm filter and cooled at 4°C overnight.

Surface modification and immobilization of diacetylene lipid vesicles on PDMS micropillars
The surface modification process is shown in Figure 32. The PDMS substrates were set in a UV-Ozone cleaner for 10 min to form hydroxyl groups. The substrates were silanized in a 4.2 mM of AEAPDMS in anhydrous ethanol for 3 h at room temperature. The substrates were rinsed five times with anhydrous ethanol and dried in the nitrogen atmosphere inside the glove box. The AEAPDMS modified substrates were incubated in a solution containing 2.5% v/v glutaraldehyde

in deionized water for 5 hrs. The substrates were washed with deionized water to remove unreacted reagents and further dried under a stream of nitrogen. The surface morphology of AEAPDMS and GA modified substrate was identified by AFM with NCHR non-contact tip, and the thickness of the resulted layer was measured by an ellipsometer. The GA formation on the quartz substrate was confirmed by using a UV/Vis/NIR spectrometer. The liposome was dried in air for 3 h. The aldehyde-modified substrates were placed in a diacetylene lipid vesicles solution for 1 h followed by rinsing with deionized water and dried under a stream of nitrogen. The immobilized diacetylene lipid vesicles were irradiated under UV light (1 mW cm^{-2}) with a wavelength of PCDA was from GFS chemicals. Sylgard 184 elastomer kit was purchased from Dow Corning and AEAPDMS was purchased from Junsei. EDEA, EDA, OTS, GA 25% in H_2O and surfactin from B. subtilis, were purchased from Sigma Aldrich.

Bacterial strains and culture condition
NCIB3610 and CU1065 were used as surfactin-producing and -defective strains of B. subtilis, respectively. For the test of Gram-negative bacterium which does not produce surfactin, E. coli DH5α strain was used. The Staphylococcus aureus Newman and Pseudomonas aeruginosa PA14 strains were used as representative pathogens of Gram-positive and Gramnegative bacteria, respectively. All of the strains were routinely grown in Lysogenic Broth (LB) with a shaking incubator (210 rpm/37∘C) for the designated incubation times as described in the results and discussion section. Bacterial growth was monitored by measuring absorbance at 600nm using UV-Vis spectrophotometer.

Fabrication of PDMS micropillars
The PDMS micropillars were fabricated using the two-step replica method. A three-dimensional pillar silicon wafer was used as the master mold. The uncured PDMS mixture (base: curing agent, 10:1 w/w) was poured on the master mold and cured at 80∘ C for an hour. After cooling down the process, the hole patterned-PDMS was detached from the master mold. Before undergoing second step molding, the hole patterned-PDMS mold was exposed to UV-ozone cleaner for 10 min to decrease the hydrophobicity for further modification. The UV-ozone treated hole patterned- PDMS molds were treated with OTS in an ethanol solution for 30 min under nitrogen atmosphere. The substrate was washed several times with ethanol. The uncured PDMS mixture was poured on the OTS treated hole patterned-PDMS mold and cured at 80∘ C for an hour. After the cooling down process, the micropillar PDMS was peeled off from the hole patterned-PDMS mold.

Preparation of diacetylene vesicles
The amine-terminated diacetylene monomers PCDA-EDEA and PCDA-EDA were synthesized by employing standard procedures. A mixture of EDEA and EDA terminated diacetylene monomers were dissolved in chloroform in a test tube. The solvent was evaporated by a stream of N2 gas, and deionized water was added to the test tube to give the desired concentration of lipid (1mM). The resultant suspension was sonicated for 15 min at 80∘ C followed by filtering for removing dispersed lipid aggregates by using a 0.8 μm filter and cooled at 4∘ C overnight.

Surface modification and immobilization of diacetylene lipid vesicles on PDMS micropillars

The PDMS substrates were set in a UV-Ozone cleaner for 10 min to form hydroxyl groups. The substrates were silanized in a 4.2 mM of AEAPDMS in anhydrous ethanol for 3 h at room temperature. The substrates were rinsed five times with anhydrous ethanol and dried in the nitrogen atmosphere inside the glove box. The AEAPDMS modified substrates were incubated in a solution containing 2.5% v/v glutaraldehyde in deionized water for 5 hrs. The substrates were washed with deionized water to remove unreacted reagents and further dried under a stream of nitrogen. The surface morphology of AEAPDMS and GA modified substrate was identified byAFM with NCHR non-contact tip, and the thickness of the resulted layer was measured by an ellipsometer. The GA formation on the quartz substrate was confirmed by using a UV/Vis/NIR spectrometer. The liposome was dried in air for 3 h. The aldehyde-modified substrates were placed in a diacetylene lipid vesicles solution for 1 h followed by rinsing with deionized water and dried under a stream of nitrogen. The immobilized diacetylene lipid vesicles were irradiated under UV light with a wavelength of 254 nm for 1 min. The morphology and size of the immobilized PDA liposome were analyzed by scanning electron microscope.

Determination of the surfactin concentration fluorescence measurement
In order to quantify the amount of surfactin produced from bacterial cells by measuring the fluorescence, cell-free culture media were directly incubated with immobilized PDA vesicles. To recover the supernatants after cell cultures, the cells were discarded by centrifugation with $15,000 \times g$ for 5 min. After immersing the immobilized PDA vesicles in the supernatants for 1 h at 25° C, the immobilized PDA vesicles were washed with ethanol and deionized water. The fluorescence microscopy images were taken from the optical microscope and analyzed by using ImageJ. To determine the detection limit of surfactin by immobilized PDA vesicles, a dose-dependent test was performed using various starting cultures with different initial concentrations of bacterial cells from 4×10^7 to 4×10^1 cells/ml. The selectivity of the immobilized PDA vesicles to the surfactin was tested using seven different strains of bacteria: B. subtilis NCIB3610, B. subtilis CU1065, B. cereus ATCC11778, B. licheniformis ATCC14580, S. aureus Newman, P. aeruginosa PA14, and E. coli DH5α. The initial inoculum with a cell density of 4×10^7 cells/ml was cultured for 24 h. The surfactin standard curve was generated using fluorescence signals obtained from the 2D or 3D-PDA-PDMS immersed in different concentrations of the standard surfactin ranging from 500 nM to 1 mM.

High-pressure liquid chromatography
The cell-free media supernatants were recovered as described above for fluorescence measurement. The concentration of surfactin in the supernatants was determined using an HPLC-UV/Vis quantification method. The analysis was performed with standard high-pressure liquid chromatography equipped with a reverse phase column at 30°C. An isocratic method was performed with 80% acetonitrile and 20% 3.8 mM trifluoroacetic acid for 25 min. The peptide bonds of the surfactin were detected at a wavelength of 210 nm.

Results and Discussion

The routine procedure for immobilizing the assembled vesicles of PCDA-EDEA and PCDA-EDA is by using GA on a solid support with a surface amine functional group. In this study,

AEAPDMS were used to generate the monolayer and amine functionalization on the surface of PDMS for uniform immobilization of glutaraldehyde. In order to obtain a preliminary clue for ensuring the formation of a monolayer on the sensor template, 2D silicon substrate, and quartz substrate were used for surface characterization. The surface properties of the amine- modified and GA modified substrate were characterized by using an ellipsometer and AFM. The measured thickness of the AEAPDMS monolayer on the Si substrate after 3h of modification was 11 ± 1 Å, and the average thickness of GA was about 8 Å which is in agreement with its theoretical thickness. Figures 32A, B showed $1.0 \times 1.0\mu m$ AFM images of the AEAPDMS modified and GA modified Si substrate, respectively. The non-contact mode AFM images did not show any aggregated multilayer formation after AEAPDMS modification with the RMS value of 0.18nm, and it was similar to RMS value after GA modification. Based on these results, the resultant layer of GA is regarded as a monolayer. However, a successful surface modification on the sensor template cannot be decided just by looking at the morphology, to confirm a successful GA modification on an AEAPDMS-modified substrate. Figure 32C shows the UV-visible spectrum of GA solution and immobilized GA on the quartz substrate where the GA has sharp characteristic absorption at 203 nm, which has been assigned to the π-$\pi*$ transition of the carbonyl groupwhereas the immobilized GA on the quartz substrate has similar sharp spectral peaks as that of the GA solution at 216 nm with a redshift of 13 nm. A successful modification of the sensor template with the GA molecules can offer the reproducibility and uniformity of immobilized diacetylene vesicles.
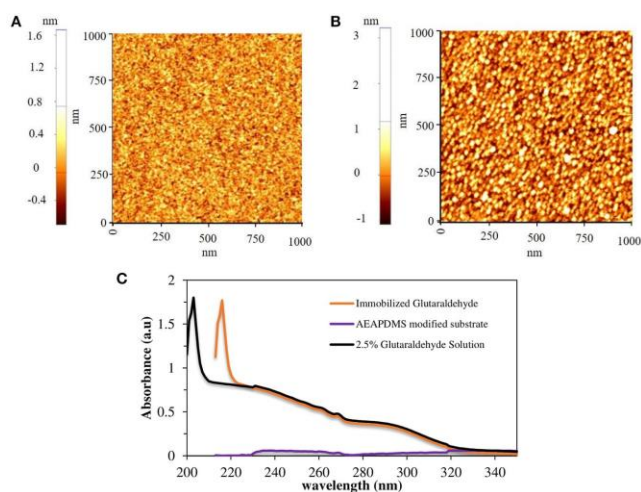

Figure 32. AFM images of (A) AEAPDMS modified substrate and (B) glutaraldehyde modified substrate, (C) UV-Vis spectra of glutaraldehyde solutions and glutaraldehyde modified quartz substrate.

A reliable biosensor platform requires structure uniformity and stability of the receptor on the sensor template. Since the diacetylene is a colloidally dispersed liposome, it can be formed as a film or vesicle during the immobilization process. However, the vesicle form has been reported to be more sensitive than the film form. Figures 33A, B show the SEM and fluorescence images of immobilized PDA on the 2D PDMS substrate in film form, while Figures 33C, D show the SEM and fluorescence images of the immobilized PDA on the 2D PDMS in vesicle form at approximately 30-80 nm in size which is in agreement with previous study. The fluorescence images were obtained after heat treatment (100∘C, 1min). The heat treatment induces a blue to the red transition of the PDA since the blue phase PDA is non-fluorescent. As presented in

Figures 33B, D, and the fluorescence intensity of the vesicle form immobilized PDA is two times higher than the film form, which is in agreement with a previous report. The vesicle form of the PDA is presumed as a spherical form that has a higher surface area than the film form of the PDA. Since there is a proportional relationship between the fluorescence intensity and surface area, the vesicle form emitted a higher intensity compared to the film form. Therefore, in this study, we selected immobilized PDA in vesicle form to develop a PDA-based label-free bacteria sensor.
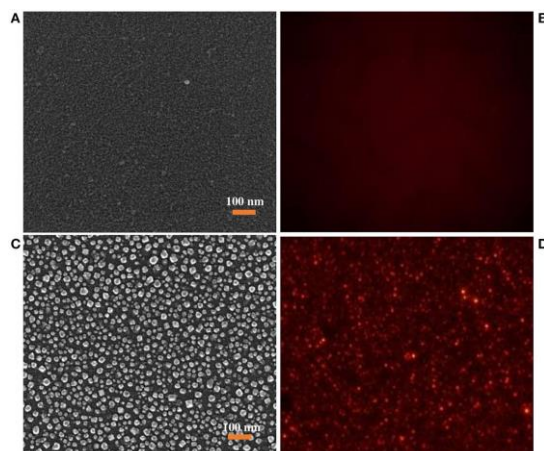

Figure 33. (A) SEM images of immobilized PDA liposome in film structure, (B) corresponding fluorescence images of Immobilized PDA liposome in film structure obtained after heating treatment, (C) SEM images of immobilized PDA liposome in vesicle structure, (D) corresponding fluorescence images of Immobilized PDA liposome in vesicle structure obtained after heating treatment.
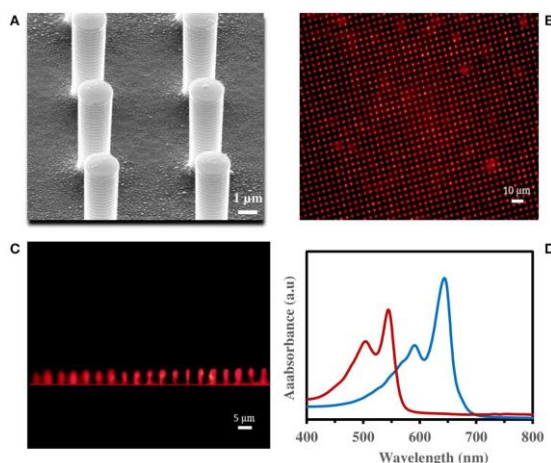

Figure 34. (A) SEM images of immobilized PDA vesicles on PDMS micropillars, fluorescence microscopic image of PDA immobilized on PDMS micropillars from (B) top view, (C) side view, (D) visible spectra of immobilized PDA vesicles on quartz substrate, before (blue line) and after (red line) 1 h incubation in 0.1 mM surfactin.

The immobilized PDA vesicles on PDMS micropillars (3D- PDA-PDMS) were also prepared under the same conditions used for the 2D PDMS substrate. The SEM images of fabricated PDMS micropillars show height, gap and diameter around 5, 4 and 2 μm respectively as presented in Supplementary Figure 33. As presented in Figure 34A, the PDA vesicles were also

immobilized uniformly on the 3D PDMS micropillars substrate. For proving a successful immobilization of PDA vesicles on the 3D PDMS micropillars substrate, fluorescence images (Figures 34B, C) and UV-visible spectra (Figure 34D) of the PDA after 0.1 mM surfactin incorporation were obtained. The fluorescence image of the top view (Figure 34B) and the side view (Figure 34C) prove the efficiency of the PDA immobilization and UV-visible spectra. Figure 34D presents a significant UV absorption shift from the blue phase (645 nm) to the red phase (545 nm) after 0.1 mM surfactin incorporation.
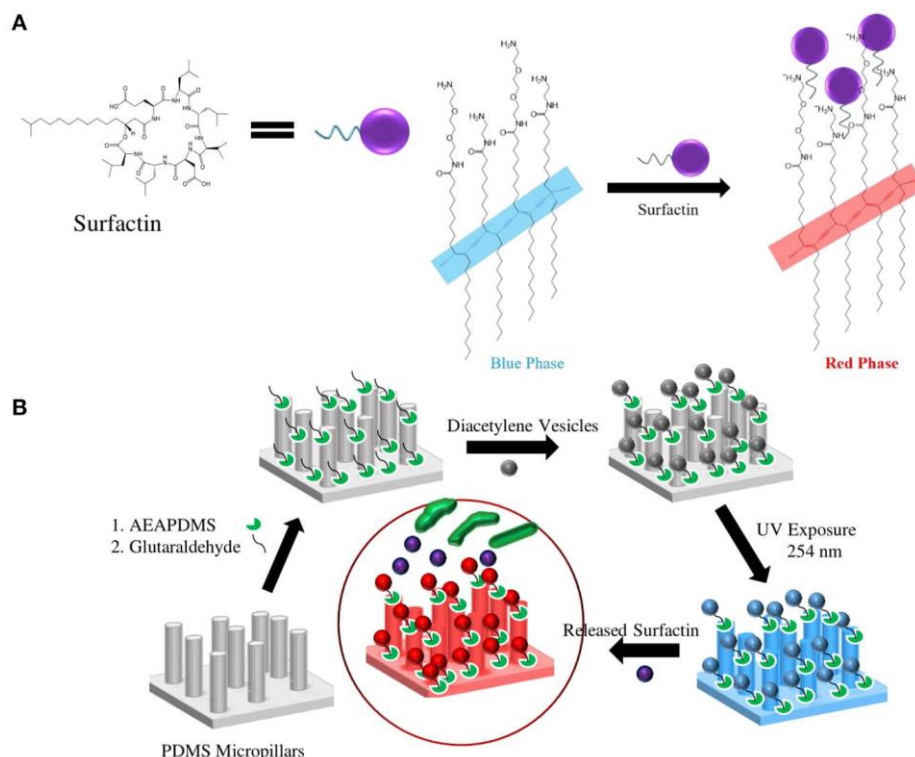

Figure 35 Schematic of (A) PDA-surfactin interaction through the ionic interaction between the hydrophilic head of surfactin and amine group of PDA and fatty acid chain of surfactin with carbon backbones in PDA, (B) procedure of surface modifications and immobilization of PCDA on the PDMS micropillars.

Figures 35A, B illustrate the surfactin based label-free bacterial sensor platform using 3D-PDA-PDMS. Thus, in pursuance of a feasible sensor platform using immobilized PDA vesicles, the 2D and 3D-PDA-PDMS were exposed to various concentrations of surfactin. As shown in Figure 36A, the fluorescence signals from the 2D-PDA-PDMS were hardly observable until 500μM of surfactin whereas a red fluorescence intensity from 3D-PDA- PDMS was significantly enhanced with increasing concentration of surfactin in a range from 5 μM to 1 mM (Figure 36B). Figure 36C displays a calibration curve which consists of plots of fluorescence intensity as a function of the surfactin concentration at log scale. The calibration curve was used for quantitative estimation of the surfactin by a linear regression model for curve- fitting analysis. The R-squared of the experimental data of the 3D-PDA-PDMS was 0.99. The detection limit of the 2D and 3D-PDA-PDMS were found to be 500 and 5μM, respectively. Thus, an increase in the sensitivity of at least 100 times was obtained with the 3D over the 2D-PDA-PDMS. These results clarify our previous study conducted using 3D networked PDA for quantification of α-cyclodextrin where the large increase in the sensitivity of the 3D-PDA system over 2D- PDA system was not only

due to the increment of the template surface area but was also caused by the significant increase in the target molecule accessibility to interact with immobilized PDA. Moreover, the immobilized PDA on the 2D system tends to form an aggregate that prevents the accessibility of the target molecules whereas the 3D system increases the accessibility of the target molecules through the ordered pathways of the 3D templates. The reproducibility of the 3D-PDA-PDMS was evaluated by repeatedly assaying using the coefficient of variation (CV, n = 3). The CV value of the 3D-PDA-PDMS was calculated to be 0.78%. A small CV value calculated at <2% for this method indicates the precision of the developed platform. In addition, the accuracy of the 3D-PDA-PDMS was observed by the standard addition method. The % recovery values for the accuracy of the 3D-PDA- PDMS on the quantification of the surfactin was calculated to be 96.8%. This complies with the % recovery values for a unit concentration of 0.5 mM. Therefore, the results of the developed platform show a good accuracy of surfactin quantification.
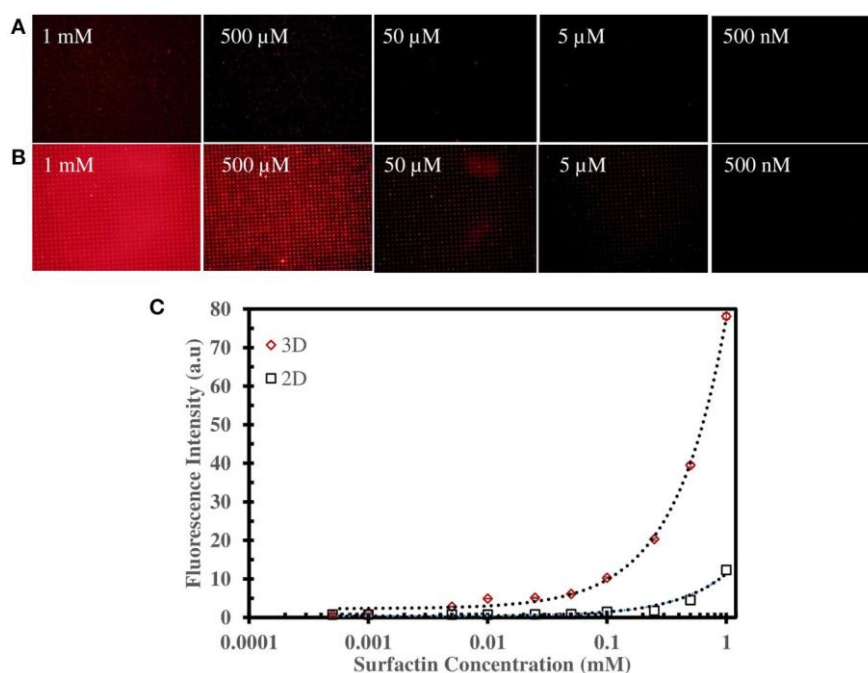

Figure 36. Fluorescence microscopic image of (A) 2D-PDA-PDMS, (B) 3D-PDA-PDMS after exposure to various concentration of surfactin, (C) plot of fluorescence intensity of PDA sensors in 2D and 3D-PDA-PDMS as a function of surfactin concentration in log scale.

To investigate the sensing ability of our platform as a label-free bacterial sensor, we first examined the surfactin-induced chromatic response using two different Gram-positive B. subtilis strains (the NCIB3610 strain as a normal surfactin-producer and the CU1065 strain as a surfactin-defective producer), as described previously. For quantitative evaluation and comparison of surfactin production during bacterial growth, both strains were cultivated in the growth medium. Cell-free media were obtained after 0, 4, 8, 12, and 24 h (Figure 37). The CU1065 strain was likely to reach a stationary phase around 12h, while the NCIB3610 strain was able to continuously grow for 24h, indicating that CU1065 achieved the maximum growth yield earlier than that of the NCIB3610 strain. Consistent with previous studies, our data also show that the production levels of surfactin have a correlation with the growth pattern where the maximum production of the surfactin occurs at the end of the exponential growth phase.

Next, to evaluate our platform as an effective bacterial detection platform, we determined the detection limit of the initial bacteria concentration by 3D-PDA-PDMS. We prepared various bacterial solutions of NCIB3610 and CU1065 strains with different initial cell concentrations ranging from 4×10^7 to 4×10^1 cells/ml. The sensor platforms were exposed to each media supernatant after 24h of cultivation, and the corresponding fluorescence intensities were measured. As shown in Figures 38A, B, even in the groups where the initial concentration was 4×10^1 cells/ml (for both NCIB3610 and CU1065), distinguishable changes of fluorescence intensity were observed compared to the control group (no cell). Furthermore, the initial cell concentrations of the surfactin- producing NCIB3610 strain displayed a strong linear positive correlation with the concentrations of surfactin (which was calculated based on the standard curve as shown in Figure 36C) produced by live cells in growth media (Figure 38C). In order to confirm our 3D-PDA-PDMS based surfactin quantification method, the data deduced in Figure 48C was further verified by direct comparison with the results obtained from the HPLC quantification method (Table 3). The results from our 3D-PDA- PDMS method were in good agreement with those using the HPLC method since the calculated t (tcal) were less than table t (ttab) with ttab of 2.45 (df = 6 and α = 0.05).
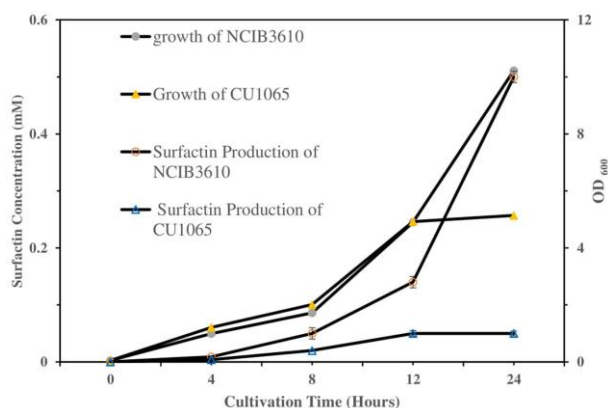

Figure 37. Comparison of the bacterial growth and surfactin production of NCIB3610 and CU1065 strains as a function of the cultivation time. Each of supernatant samples was analyzed by HPLC.

As described above, despite the similar cell concentration, our 3D-PDA-PDMS platform exhibited a significant difference in color changes between surfactin-producing NCIB3610 and surfactin-defective CU1065 strains. This observation strongly suggests that other chemicals, except for surfactin, produced by bacteria are not efficiently sensed by our 3D-PDA-PDMS platform. To further investigate the specificity of the 3D-PDA- PDMS platform to surfactin, five additional well-characterized bacteria were selected: B. licheniformis ATCC14580 [close relative to B. subtilis and surfactin-positive], B. cereus ATCC11778 (surfactin-lacking Bacillus strain), S. aureus Newman (surfactin-lacking Gram-positive pathogenic bacterium), P. aeruginosa PA14 (surfactin-lacking Gram-negative pathogenic bacterium), and E. coli DH5α (surfactin-lacking Gram-negative model bacterium). After cultivation of the cells for 24 h, their media supernatants were then exposed to 3D-PDA-PDMS, followed by observation of fluorescence images. As expected, only our 3D-PDA-PDMS incubated with cultured media from B. licheniformis exhibited a notable color change, whereas no remarkable change was observed for the other tested strains (Figure 39). Since there was no significant difference in the growth yield between the surfactin-producers and non-surfactin-producers, the color change detected by our 3D-PDA-

PDMS seems to be mainly due to the presence of surfactin rather than the other chemicals produced by the cells.
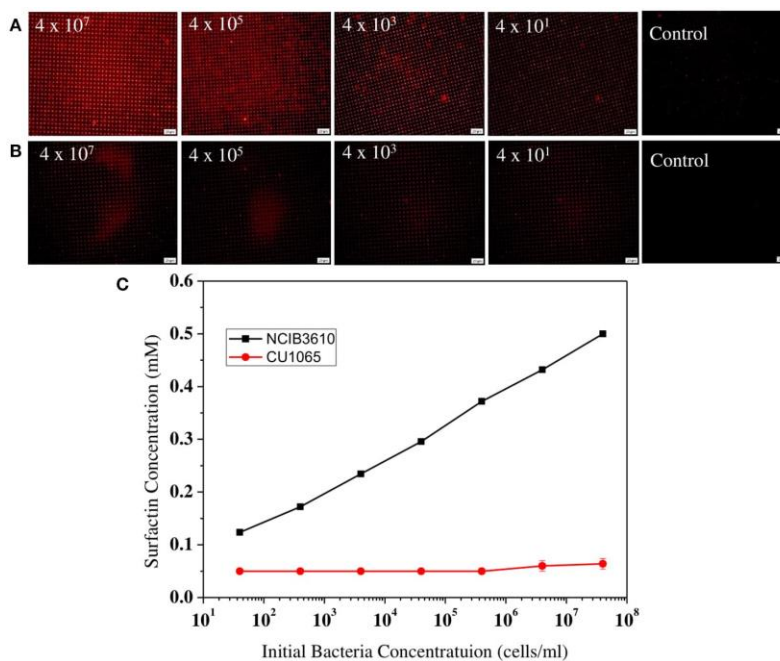

Figure 38. Comparison of the surfactin-detecting sensitivities between B. subtilis NCIB3610 and B. subtilis CU1065. The fluorescence images of sensor platform after exposed to media supernatants of (A) NCIB3610 strain and (B) CU1065 strain, (C) Plot of 3D-PDA-PDMS measurement of surfactin production levels depending of the initial cell concentrations.

Table 3. Quantification and comparison of surfactin levels measured by using the immobilized PDA lipid vesicles and HPLC method.

Initial Bacteria Concentration (cells/ml)	NCIB3610 (mM)		CU1065 (mM)	
	3D-PDA-PDMS	HPLC	3D-PDA-PDMS	HPLC
4×10^7	0.45	0.5	0.064	0.08
4×10^6	0.42	0.43	0.06	0.067
4×10^5	0.37	0.4	0.05	0.06
4×10^4	0.29	0.3	0.05	0.06
4×10^3	0.24	0.25	0.05	0.055
4×10^2	0.17	0.18	0.05	0.05
4×10^1	0.12	0.13	0.05	0.05

NCIB3610 and CU1065 strains of B. subtilis were inoculated with different amount of initial cells.
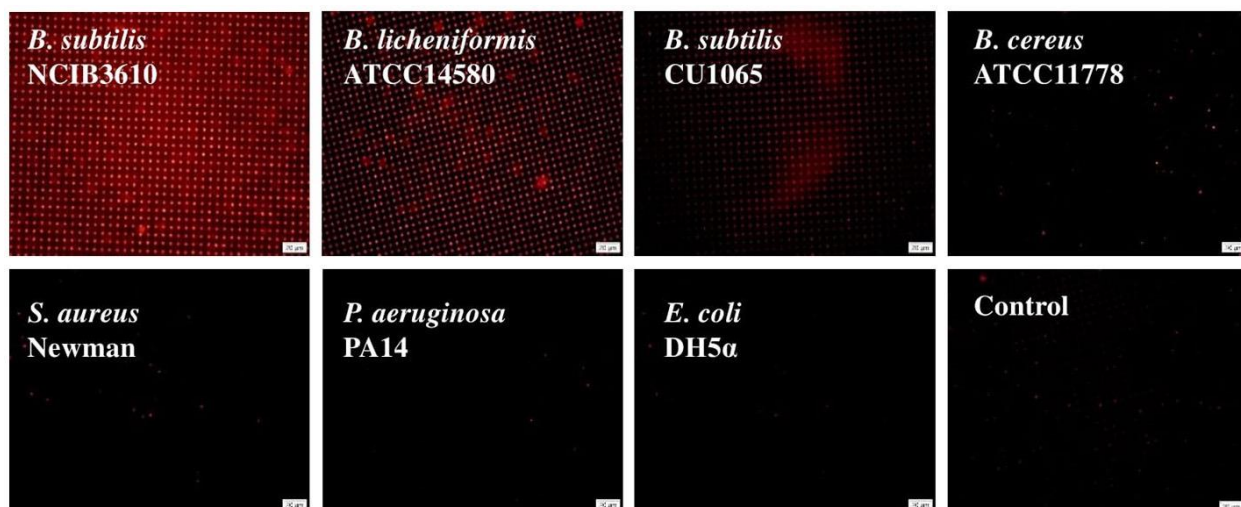
Figure 39. Fluorescence images of sensor platform after exposed to the media supernatant of different bacterial strains which were grown in LB for 24 h.

Conclusion

We investigated a sensitive and reproducible 3D-PDA-PDMS for a surfactin-based label-free bacteria sensor by utilizing the chromatic response of immobilized amine functionalized PDA. The surface of amine-modified PDMS was uniformly modified with glutaraldehyde for facilitating PDA immobilization. The potential applications of 3D-PDA-PDMA as a feasible bacterial sensor was studied through quantitative analysis of surfactin. The sensitivity of 3D-PDA-PDMS was approximately 100 times higher than that of the 2D-PDA-PDMS. The sensitivity enhancement of the 3D-PDA-PDMS was caused by the increment of total binding sites and the facile accessibility of the target molecules. The 3D-PDA-PDMS system can detect the presence of 5 μM surfactin and the initial presence of 4×10^1 cells/ml of Bacillus subtilis NCIB3610 which actively produce surfactin. Furthermore, the bacterial strains known to produce no surfactin were not detected by 3D-PDA-PDMS. It is therefore suggested that 3D-PDA-PDMS is highly specific to surfactin. The sensing ability of the 3D-PDA-PDMS was assessed through a comparison with the standard HPLC method. The results of the surfactin concentration produced by bacteria measured by 3D-PDA-PDMS were in agreement with those measured by HPLC.

List of Publications and Significant Collaborations that resulted from your AOARD supported project

a) papers published in non-peer-reviewed journals and conference proceedings

1. Gedi, V.; Song, C. K.; Kim, G. B.; Lee, J. O.; Oh, E.,; Shin, B. S.; Jung, m.; Shim, J.; Lee, h.; Kim, Y. P., Sensitive OnChip Detection of Cancer Antigen 125 Using a DNA Aptamer/Carbon Nanotube Network Platform, Sensors&Actuators B: Chemical, 2018, 256, 89-97
2. Song, C. K.; Oh, E.; Kang, M. S.; Shn, B. S.; Hn, S. Y.; Jung, M.; Lee, E. S.; Yoon, S. Y.; Sung, M. M.; Ng, W. B.; Cho, N. J.; Lee, H., Fluorescence-Based Immunosensor using Three-Dimensional CNT Network Structure for Sensitive and Reproducible Detection of Oral Squamous Cell Carcinoma Biomarker, Analytica Chimica Acta, 2018, 1027, 101-108
3. Chen, R.; Kang, J.; Kang, M.; Lee, H.; Lee, H., Silicon Pillar Structure Assisted three Dimensional Carbon Nanotube Assembly: Fabrications and Rational Surfce Modifications, Bulletin of the Chemical Society of Japan, 2018, 91, 6, 979-990
4. Jannah, F.; Kim, J. H.; Lee, J. W.; Kim, J. M.; Kim, J. M.; Lee, H., Immobilized Polydiacetylene Lipid Vesicles on Polydimethylsiloxane Micropillars as Surfactin-based Label-free Bacterial Sensor Platform, Front. Mater., 2018, 5:57
5.

b) conference presentations without papers - none

1. Chen, R.; Song, C. K.; Kang, M. S.; Shin, B. S.; Lee, H.; Lee, H., Hierarchical Three Dimensional Nanostructures Based on Carbon Nanotubes for Sensor Platform, University of Houston International Symposium on Chemical Sciences, 2017.
2. Chen, R.; Han, S.; Lee, H.; Kang, J.; Lem, J.; Jung, G.; Cho, S.; Lee, H., Fabrication of Array of Hierarchical Carbon Nanotube Nanostructures on Si Micro Pillars Pattered Substrates, IC ME&D 2017, 2017.
3. Kang, H.; Song, C. K.; Chen, R.; Jung, M.; Shim, J.; Fadilatul, J.; Leem, J.; Lee, H., Cancer Biosensor Microfluidic System Bades on the Three-Dimensional Web Structure of Carbon Nanotubes, NANO KOREA 2017, 2017.
4. Shim, J.; Jung, M.; Lee, H.; Kang, J.; Jannah, F.; Chen, R.; Song, C, K.; Lee, H., A Three-dimensional Network of Carbon Nanotube Template Incorporated onto Microfluidic Platform for Cancer Biomarker Detection, Chemosensor 2017, 2017.
5. Chen, R.; Song, C. K.; Kang, M. S.; Shin, B. S.; Han, S.; Lee, H., Hierarchical Three Dimensioanl Structure Based on Carbon Nanotubes for Sensor Platform Application, HYU-TiTech Joint Workshop 2016, 2016.
6. Lee, H.; Chen, R.; Han, S.; Song, C. K.; Kang, M. Shin, B.; Lee, S., A Novel Sensor and Catalysis Platform Based on Hierarchically Ordered Three-dimensional Network of Carbon Nanotubes, Gordon Research Conference; Multifunctional Materials & Structures, 2016.
7. Han, S. Y.; Chen, R.; Shin, B. S.; Song, C. K.; Kang, M.; Lee, H. D.; Lee, H., A Novel Platform Based on Hierarchically Ordered Three-dimensional Network of Carbon Nanotubes, IC ME&D 2016.

c) Provide a list any interactions with industry or with Air Force Research Laboratory scientists or significant collaborations that resulted from this work.